Karlsruhe Institute of Technology

Reflexionsseismische Datenanalyse des Russell-Gletschers, Grönland

Reflection Seismic Data Analysis of Russell Glacier, Greenland

Bachelor's Thesis of

Betty Heller

At the Faculty of Physics
Geophysical Institute

Reviewer:	Prof. Dr. T. Bohlen
Second Reviewer:	Prof. Dr. O. Eisen
Supervisor:	Dr. C. Hofstede

Duration: 01.08.2016 – 08.11.2016

Declaration

I hereby declare that I have developed and written the enclosed thesis independently, and have not used sources or means without declaration in the text. Any work of others or literal quotations are clearly cited.

Karlsruhe, 08.11.2016, _____

Betty Heller

Approved as sample copy by

Karlsruhe, 08.11.2016, _____

Prof. Dr. T. Bohlen

Table of Contents

1 Summary

Modelling the glacier dynamics of the Greenland Ice Sheet is a central part of climate research. To be able to model the processes that influence a glacier's flow, the position of its ice-bed contact is a basal boundary condition.
Using five different P-wave reflection seismic datasets, the subsurface structure of Russell Glacier, which is a land-terminating glacier in southwest Greenland, is investigated. The data have been recorded by the glaciology group of the Alfred-Wegener Institute, in the ablation zone of Russell Glacier.

To investigate the efficiency of the minivibrator source ELVIS III on polar glaciers having ice thicknesses up to several kilometers, a dataset using the ELVIS source is compared to an equivalent explosive seismic dataset. The question to answer is, if the approximately 600 m deep glacier bed and additional subglacial structures are displayed by the vibroseis data.
As the maximally 10-fold vibroseis data, in contrast to the maximally 2-fold explosive seismic data, don't reveal any reflection signals, it is concluded that the penetration depth of the ELVIS signal is too small to resolve subglacial structures on polar glaciers.

The subsurface structure of the survey area is investigated with the help of two explosive seismic datasets. In the resulting depth profiles lying perpendicular to each other, a distinct topography of the glacier bed as well as a stratification of the subglacial material is visible.
The propagation velocities of seismic P-waves in the subsurface layers are firstly determined by applying Dix' method at two additional explosive datasets. As the subglacial material couldn't be determined that way, for the reason that the appurtenant velocity value determined with Dix' method are not reliable due to the topography of the covered reflector, the polarity of the reflection coefficient associated with the first layer boundary are reconstructed using the material classification from Christianson et al. (2014).
For future applications of Dix' method in order to determine seismic velocity values, a preliminary processing of seismic data in the field would be productive to be able to record the additional common-midpoint datasets in preferably horizontal stratified areas.

The resulting two-layer subsurface model finally consists of the top 500-600 m thick ice pack with P-wave velocities in the range of $v_1 = 3500-3700\,\mathrm{m\,s^{-1}}$ and below lying subglacial sediments with P-wave velocities in the range of $v_2 = 1700 - 1900\,\mathrm{m\,s^{-1}}$, corresponding to unconsolidated sediments or dilatant till. The orthogneiss forming the bedrock in the survey area (Klint et al., 2013) couldn't be resolved by the used seismic datasets, from which it can be inferred that its depth amounts to more than 600 m.

2 Introduction

In this thesis, five P-wave reflection seismic datasets recorded on Russell Glacier, southwest Greenland, are processed and interpreted. For one of them, the minivibrator source ELVIS III (Electrodynamic Vibrator System) was used as seismic source, for the others, dynamite in boreholes was used.

As Russell Glacier is a land-terminating glacier, the interaction of the melting and the ice flow velocity can be investigated in its ablation zone without incorporating oceanic influences. Measuring melting rates, basal water pressure and ice velocities in the ablation zone of Russell Glacier, van de Wal, Smeets, et al. (2015) reveal that the formation of a network of meltwater channels during summer decelerates the ice flow.
In the current thesis, the subglacial structure of Russell Glacier is investigated, as the ice-bed contact represents a basal boundary condition for ice flow models.

The first question to investigate is if the ice-bed reflection and some subglacial stratification can be observed in the vibroseismic data. Up until now, ELVIS has effectually been applied on low-depth (approximately 60 m thick) alpine glaciers, see Diez et al. (2014). Due to the higher productivity of the vibroseis method compared to borehole-explosive seismics (Hofstede et al., 2013), the efficiency of the ELVIS source on polar glaciers which have ice thicknesses up to several kilometers is investigated as a basis for future applications.

The second aim of the current work is to derive boundary conditions for the subglacial model of the survey site used for ice flow modeling. From two perpendicular seismic profiling lines, structural features of the glacier bed are investigated. On top of that, seismic P-wave velocities are determined as material parameters by applying Dix' method to the remaining two common-midpoint (CMP) datasets, and reconstructing the changes of sign of the reflection coefficient visible in the profiling datasets, using the material classification from Christianson et al. (2014).

3 Glaciological Overview

3.1 Glaciological Fundamentals

3.1.1 Glacier Zones and the Formation of Ice

This section introduces the glaciological terms used in the current thesis. Its content is extracted from Paterson (1994).

A glacier can be divided into an accumulation area, where mass is accumulated over a year, and an ablation area with a net mass loss of the glacier. Figure 3.1 shows the subdivision of a glacier in the dry-snow zone, the percolation zone, the wet-snow zone and the superimposed-ice zone which are part of the accumulation area, bordered by the equilibrium line from the ablation area. The way ice develops from snow and the duration of this process depends on the temperature. In the dry-snow zone, the temperature remains below the melting point during the entire year and ice develops through sintering. Thereby, the snow is densified by several processes including relative particle movement, sublimation, recrystallization and deformation. In the intermediate stage between snow and ice, the material is called firn. The distinction between firn and ice is drawn at a density of $830\,\mathrm{kg\,m^{-3}}$, when the contained air is sealed off in bubbles.
In the percolation zone, ice layers, lenses and glands form through refreezing of meltwater percolated into the snow layer. Due to the latent heat released by this process, the surrounding snow is warmed up to the melting point which accelerates the formation of ice.
In the adjacent wet-snow zone, the total amount of the last year's fresh snow is raised to the melting point at the end of the summer.
In the percolation zone and the wet-snow zone, snow, firn and ice occur in alternating layers (and in other shapes such as lenses or patches, respectively). The superimposed-ice zone consists of a continuous ice mass as enough meltwater yields a merging of the ice layers.
The ablation zone is characterized by melting water run-off, evaporation and snow blown away by wind.

3.1.2 Subglacial Bedforms

Below moving glaciers, sediments are deposited and deformed resulting in various shapes of subglacial bedforms, which are described by Benn and Evans (1998):

Drumlins, flutings and megaflutings are elongated sediment accumulations arranged parallel to the glacial ice flow, and are distinguished by their elongation ratio (i.e.

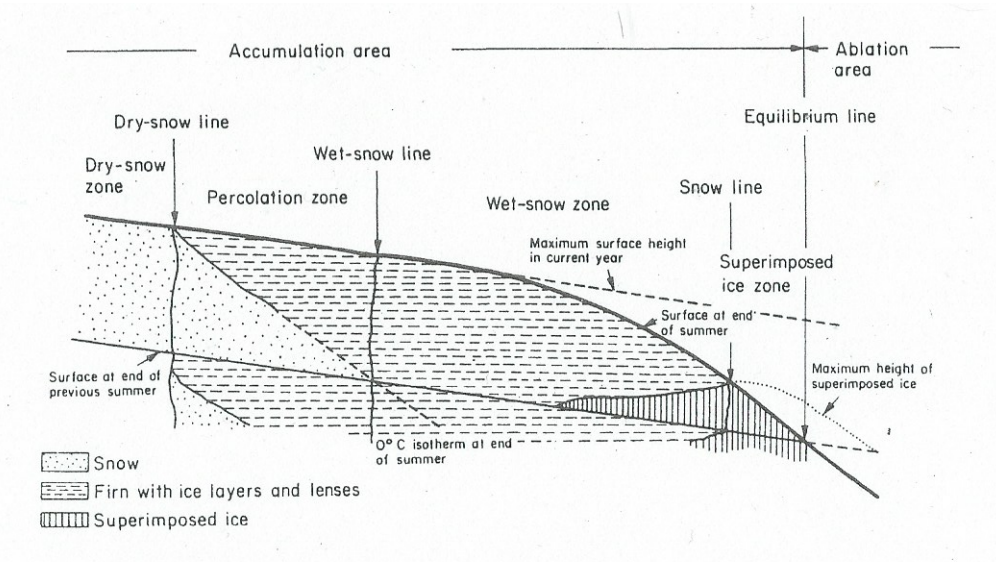

Figure 3.1: Glacier zones, extracted from Paterson (1994).

the length-to-width ratio) as well as their absolute length.
Drumlins are more than 100 m long and have an oval shape, their elongation ratio can reach up to 7:1. Their luv side with respect to the ice flow is steeper than their lee side which has on top of that a pointed shape. Flutings have a smaller length than drumlins, they however have greater elongation ratios ranging from 2:1 to 60:1. Finally, the length of megaflutings is greater than 100 m, with elongation ratios similar to those of flutings.
In contrast to the mentioned bedforms, Rogen moraines are arranged transversely to the ice flow. Their shape resembles coalescent arcuate ridges with heights up to 30 m and widths up to 100 m.
The mentioned bedforms are formed below moving ice sheets. The exact formation mechanisms are explained by several theories of which Benn and Evans (1998) gives an overview.
Another subglacial association, having the shape of sinuous ridges, are eskors. They are the sediment infillings of glacial drainage channels and form through sediment deposition.

Generally, all subglacial bedforms occur in groupings and the transition between the designations is gradual.

3.2 Glaciological and Geological Features of the Considered Site

3.2.1 The Greenland Ice Sheet

The Greenland Ice Sheet covers an area of 1.71×10^6 km^2 and consists of a 2.85×10^6 km^2 ice volume (Rignot and Mouginot, 2012).
Moon and Joughin (2008) give a classification of Greenland's outlet glaciers based

on their terminus type: Ice-shelf glaciers lose mass at a calving front being longer than 10 km, and are therefore characterized by advancing or retreating in particular episodes. Tidewater glaciers are also marine-terminating and end by a floating ice tongue. According to Rignot and Mouginot (2012), they drain 88 % of the Greenland Ice Sheet's area.
In contrast to the two mentioned marine-terminating glacier types, the ice front of land-terminating glaciers isn't observed to change appreciably (Moon and Joughin, 2008). According to Moon and Joughin (2008), land-terminating glaciers with a width greater than 2 km are most concentrated in southwest Greenland.

3.2.2 Russell Glacier

Russell Glacier is a land-terminating glacier in southwest Greenland (Smeets et al., 2012). The examined data have been collected on the site SHR, which is part of the Kangerlussuaq-transect (K-transect) and is located in the ablation zone of Russell Glacier (van de Wal, Smeets, et al., 2015). As described in van de Wal, Boot, et al. (2012), the K-transect lies perpendicular to the ice front of Russell Glacier and comprises eight measuring stations located between the ice margin and 140 km towards the interior of the ice sheet. Especially, meteorological and mass balance measurements, as well as ice velocity measurements by GPS are conducted (van de Wal, Boot, et al., 2012). SHR is located approximately 15 km away from the glacier's margin and 35 km from the locality Kangerlussuaq, as seen in Fig. 3.2.
According to Klint et al. (2013), the bedrock in this area is Archaean orthogneiss.
The surface ice flow is directed from east to west (274.5°) and amounts to $52.26 \pm 0.01\,\mathrm{m\,yr^{-1}}$ (mean rate 2008-2013, location 140 km from the ice margin of the Russell Glacier (Doyle et al., 2014)). As Russell Glacier is land-terminating, the ice flow isn't directly affected by oceanic currents.
The ice surface at SHR is hilly and doesn't exhibit lakes after the melting season in summer. Instead, meltwater is drained through a subglacial channel network, the efficiency of which increases during the melting season, which results in a deceleration of the ice flow (van de Wal, Smeets, et al., 2015). With regard to the processing of seismic data, the inhomogeneity of the ice bulk due to crevasses and meltwater drainages causes inaccuracies, e.g. in determining seismic velocities.

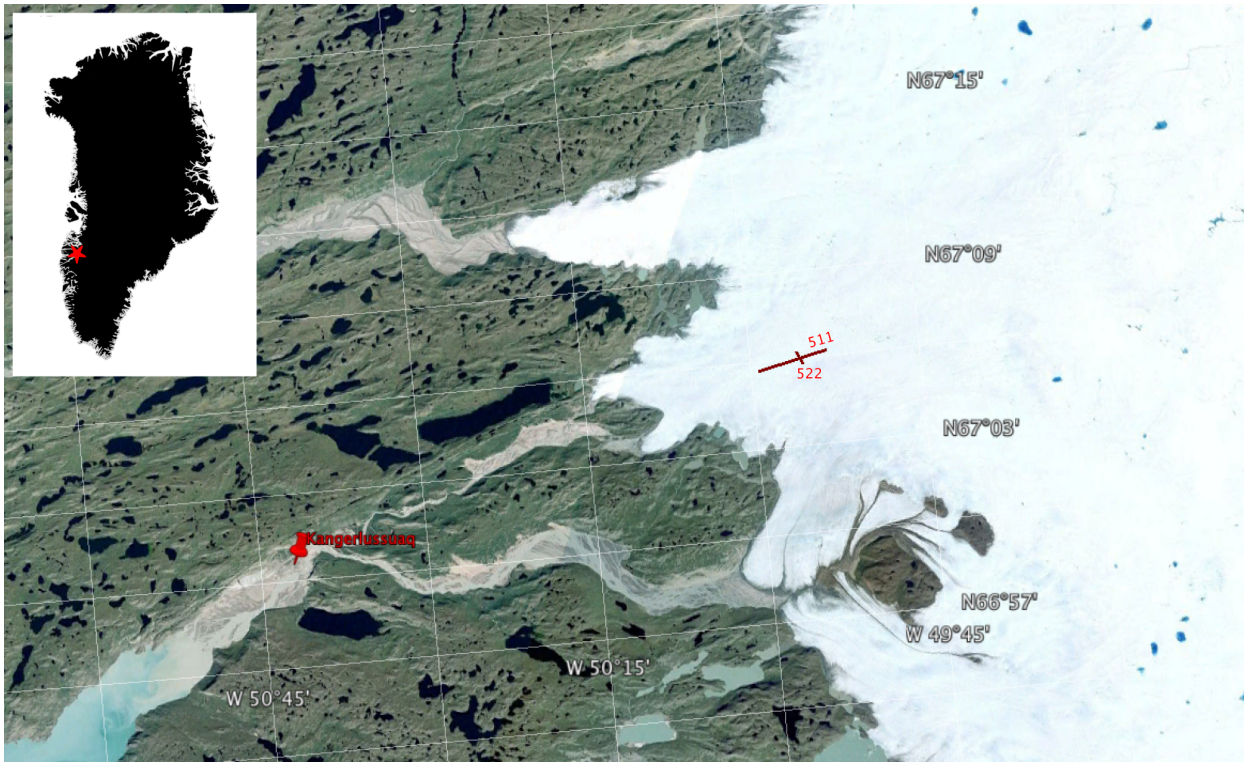

Figure 3.2: Survey site and location of the seismic lines 511 and 522 on Russell Glacier, near Kangerlussuaq. The inset displays the silhouette of Greenland with the position of Russell Glacier marked with a star.

4 Fundamentals of Reflection Seismics

4.1 Seismic Wave Propagation

The following introduction into seismic wave propagation is based on the description given by Dobrin and Savit (1988).

Seismic waves are elastic waves propagating through the earth. A distinction is drawn between body waves such as compressional and shear waves on the one hand, and surface waves such as Love and Rayleigh waves on the other hand.
Body waves are characterized by their propagation through the earth's body. In compressional waves, which are also called P-waves, the particle motion takes place in the direction of propagation. The particle motion in shear waves, which are also called S-waves, is perpendicular to the direction of propagation. The propagation velocities v_P and v_S of P-waves and S-waves, respectively, depend on the elastic parameters of the propagation medium as follows:

$$v_P = \sqrt{\frac{k + \frac{4}{3}\mu}{\rho}} \tag{4.1}$$

and

$$v_S = \sqrt{\frac{\mu}{\rho}} \, . \tag{4.2}$$

Here, k designates the bulk modulus, μ the shear modulus and ρ the density of the material.
Surface waves travel along the free earth's surface. In Rayleigh waves, the particle motion is elliptical, retrograde and takes place in a vertical plane. In Love waves, the particle motion is horizontal and perpendicular to the direction of propagation.

In active seismics, seismic waves are generated by an artificial source, such as a hammer, an explosion, an airgun or a vibrator. The receivers, called geophones or hydrophones, measure the resulting ground motion at the earth's surface.
In the case of reflection seismics, the signal of the wave reflected at subsurface interfaces, where physical properties change, is considered. With the knowledge of the travel time t, the propagation velocity v and additional information such as the geological features of the surveyed area, the subsurface structure can be modeled.

4.2 Reflection Seismic Data Acquisition

4.2.1 Explosive and Vibrator Sources

As in the considered survey dynamite and vibroseis are used as seismic energy sources, this section gives a short overview of the features of these energy sources, based on Dobrin and Savit (1988).
The original method to generate seismic waves in seismic prospecting is to detonate a dynamite charge in a borehole. Thereby, an impulsive seismic signal is generated, the frequency content of which can't be controlled, but is influenced by the composition of the propagation medium, the charge size, the hole depth and other parameters. The waveform of displacement induced by a narrow shot pulse is symmetrical at great distances and is called a Ricker wavelet.
The vibroseis signal has the shape of a sweep, which is a sinusoidal oscillation persisting several seconds, with a frequency continuously alternating in time. It is tapered on both ends to avoid Gibbs phenomena (Yilmaz, 2001). The preprogrammed signal is produced by a vibratory source consisting of a mass with a hydraulic vibrator.

The use of an explosive or a vibratory source has various advantages and drawbacks, as summarized by Hofstede et al. (2013):
Explosive seismic data provides a better resolution because of its source's broader bandwidth. This results in a clearer visibility of reflections. On the other hand, the insertion of explosive chemistry into the ground involves pollution and requires handling with dangerous substances.
An advantage of the vibroseis technique is its reproducibility and the controllability of the source signal. On top of that, it is a fast and productive method as fewer people are involved in the survey and no boreholes have to be drilled for the source as it is the case with explosives.

4.2.2 Functionality of geophones

Electromagnetic geophones base on the principle of electromagnetic induction. They consist of a magnet and a coil of wire, one of them fixed to the earth's surface, the other, being inertial, connected by a spring to the first. By the relative motion of the coil and the magnet, an electric potential difference proportional to the motion velocity is induced.
To attenuate the geophone oscillation, which is important to avoid a strong gain of the natural frequency in the resulting signal, the geophone case is filled with oil or the system is electrically damped.
Beside the natural frequency, geophones also have spurious frequencies, which are, according to Faber and Maxwell (1997), resonance frequencies above the natural frequency which are caused by oscillations along axes which are perpendicular to the working axis of the geophone.
In active seismics, several geophones are positioned at regular intervals along a cable connecting them, forming a streamer.

4.3 Mathematical Fundamentals of Reflection Seismic Data Processing

The following section about the mathematical basics of data processing in reflection seismics originates mostly from Yilmaz (2001), except for a few notation changes.

4.3.1 Fourier Transform

Digital seismic data are time series which can be expressed by a sum of sinusoids of different frequencies f, amplitudes and phase-lag.
The discrete Fourier Transform of a time series $y(n \cdot \Delta t)$ ($n \in [0, \infty)$ and the sampling interval Δt) constitutes the spectral analysis of y and can be derived from the continuous Fourier Transform by replacing the integral with a sum sign:

$$Y(f) = \int_{-\infty}^{\infty} y(t)\ \exp(-ift)\ \mathrm{d}t \ \xrightarrow{t=n\Delta t}\ Y(f) = \sum_{n=0}^{N} y(n\Delta t) \exp(-ifn\Delta t)\ . \quad (4.3)$$

As a seismic dataset consists of many time series recorded at particular offsets x, the 2-D discrete Fourier Transform applies:

$$Y(k, f) = \iint y(x, t)\ \exp(ikx - ift)\ \mathrm{d}x\ \mathrm{d}t \quad (4.4)$$

and thus

$$\xrightarrow[x=m\Delta x]{t=n\Delta t}\ Y(k, f) = \sum_{n=0}^{N} \sum_{m=0}^{M} y(n\Delta t, m\Delta x)\ \exp(ikm\Delta x - ifn\Delta t)\ , \quad (4.5)$$

where k is the wave number which is the variable of the Fourier Transform over space dimension.

In the f-k domain, plane waves appear as events with constant dips. This is used in reflection seismic data analysis to eliminate coherent linear noise by applying a frequency-wavenumber filter (f-k filter) in the f-k domain, before transforming the data back into the t-x domain which involves the application of the 2-D inverse Fourier Transform:

$$y(x, t) = \iint Y(k, f)\ \exp(-ikx + ift)\ \mathrm{d}k\ \mathrm{d}f \quad (4.6)$$

which becomes by discretization

$$y(x, t) = \sum_{n=0}^{N} \sum_{m=0}^{M} Y(m\Delta k, n\Delta f)\ \exp(-ixm\Delta k + itn\Delta f)\ . \quad (4.7)$$

4.3.2 Deconvolution, Stacking and Migration

According to Yilmaz (2001), deconvolution, stacking and migration are the main steps in seismic data processing, provided a model for the seismic velocities in the subsurface is given.

Deconvolution:
Spiking deconvolution compresses the source wavelet contained in the recorded data into a spike. Thereby, temporal resolution increases.
The following formula gives the signal model of a recorded seismic trace $y(t)$:

$$y(t) = w(t) * e(t) + n(t) \tag{4.8}$$

with w representing the basic seismic wavelet, e the earth's impulse response, n the random ambient noise and $*$ the sign for convolution, respectively. Neglecting the noise n, the deconvolution problem yields

$$y(t) = w(t) * e(t) \tag{4.9}$$

which has to be resolved.
If the source waveform is known, the solution of Eq. (4.9) becomes deterministic, and with a filter operator $f(t)$ defined by

$$e(t) = f(t) * y(t) \ , \tag{4.10}$$

the deconvolution filter follows with

$$f(t) = \delta(t) * \frac{1}{w(t)} \tag{4.11}$$

as the inverse of the wavelet.

As the source waveform is usually unknown, the solution of Eq. (4.9) is statistical and is given by the Wiener prediction theory. A Wiener filter is designed using the crosscorrelation of the zero-lag spike, which is the desired output of the filtered reflection, and the input seismogram as well as the autocorrelation of the latter.
The output, which is generated by the seismic trace $y(t)$ and the designed Wiener filter $f_W(t)$ only resembles the desired zero-lag spike if the contained seismic wavelet is minimum phase. This implies that the wavelet's energy is mostly concentrated at the beginning of its duration. Generally, the spiking deconvolution operator corresponds to the inverse of the wavelet's minimum phase equivalent.

As the spiking deconvolution operator is an inverse filter similar to the inverse amplitude spectrum of the source wavelet, as it can be seen in Eq. (4.11), a prewhitening is necessary. That is, a certain percentage of white noise (i.e. noise with a constant power spectral density) is added to the signal in order to avoid a generation of frequencies in the signal which were not there before. After that, the filter is designed from the seismogram using a time frame around the reflection visible in the data. Finally, the created deconvolution filter is applied to the data.

To suppress multiple reflections in the data, there exists also the predictive deconvolution which is not required in this work.

Stacking:
Normal Moveout (NMO) designates the two-way travel time (TWT) difference Δt between the reflection event at zero-offset $x = 0\,\mathrm{m}$ and at a given offset x. The NMO correction reduces the moveout effect from the seismic traces which thereby become stretched. After NMO correction, the reflections in a Common-Midpoint gather (CMP gather) are flattened. A CMP gather is composed of all seismic traces with the same source-receiver midpoint.

The process of stacking then sums the NMO corrected traces within the same CMP gather. This results in an increase of the Signal-to-Noise ratio because of constructive interference of coherent signal contents and destructive interference of incoherent noise, respectively.

As the NMO-correction requires the knowledge of the normal moveout Δt as a function of the offset x, while only x is known, being the distance between source and receiver, an appropriate model for the seismic propagation velocities is necessary. The velocity term used for this model is introduced in section 4.3.4.

Migration:
In the seismic stack, the stacked traces are sorted by their related CMP. The reflections in a seismic stack are displayed assuming the reflection energy to reach the geophones at normal incidence, coming from a common depth point (CDP) which lies vertically beneath the CMP. Since this is not the case if the reflector is not a horizontal layer boundary, the geometric effect of non-vertical arriving reflection energy has to be corrected. This is done by migration. It yields a representation of the subsurface along the seismic line, either in offset-time coordinates, which is done by time migration, or in offset-depth coordinates, which is done by depth migration. In doing so, migration improves the resolution along the offset-axis.

Migration principles base on the knowledge about what reflector shapes cause what features in a seismic stack. Here are some examples:
A point reflector in the subsurface is displayed as a hyperbola in a seismic stack. For this reason, hyperbolic structures in a stack are reduced to their apex by migration. Synclines, in contrast, form bow ties in the stack which can also be reversed by migration. As dipping horizons in the ground appear too flat in the stack, migration turns them into steeper dipping events.

To determine a reflector plane's dip φ from the unmigrated stack, the following relation, stated by Yilmaz (2001), can be used:

$$\frac{\Delta\tau}{\Delta x} = \frac{\Delta t}{\Delta x}\frac{1}{\sqrt{1-\left(\frac{v\Delta t}{2\Delta x}\right)^2}}\,. \tag{4.12}$$

In Eq. (4.12), $\frac{\Delta\tau}{\Delta x}$ and $\frac{\Delta t}{\Delta x}$ denote the reflector's dip in the time section after and before the migration, respectively. v is the seismic velocity in the medium. The

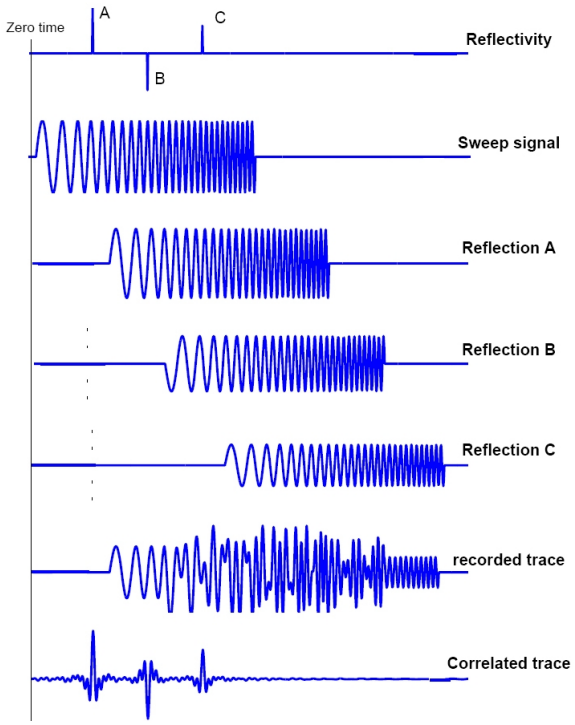

Figure 4.1: Neglecting noise and the unknown components of the initial wavelet, a vibroseis seismogram consists of the time-delayed sweeps reflected at the earth's layers. Cross-correlation with the source signal yields an interpretable signal resembling the seismogram of an impulsive source. Extracted from Ikelle and Amundsen (n.d.).

angle of the reflector plane then follows as

$$\varphi = \arctan\left(\frac{v\Delta\tau}{2\Delta x}\right) . \tag{4.13}$$

4.3.3 Vibroseis Data Processing

According to Yilmaz (2001), the vibroseis seismogram $y(t)$ can mathematically be described by the convolution of the source sweep $s(t)$ with the seismic wavelet $\tilde{w}(t)$, which again is convolved with the earth's impulse response $e(t)$:

$$y(t) = s(t) * \tilde{w}(t) * e(t) . \tag{4.14}$$

To be precise, $s(t)$ is the known component of the wavelet in contrast to the unknown component $\tilde{w}(t)$ which includes effects on the wave's propagation path as well as the recording system's response. That is, the basic wavelet $w(t)$ in Eq. (4.8) equals $s(t) * \tilde{w}(t)$ in Eq. (4.14).
Figure 4.1 illustrates the step of cross-correlation of the recorded signal with the source signal. According to Dobrin and Savit (1988), this step is necessary to be able to interpret the seismogram, and involves the comparison of $y(t)$ with the vibroseis sweep $s(t)$ at different time delays. As shown in Fig. 4.1, the recorded trace includes the sum of all the reflected arriving waves (reflections A to C) which are delayed by their TWT. As the recorded signal has thus a partial similarity to the sweep

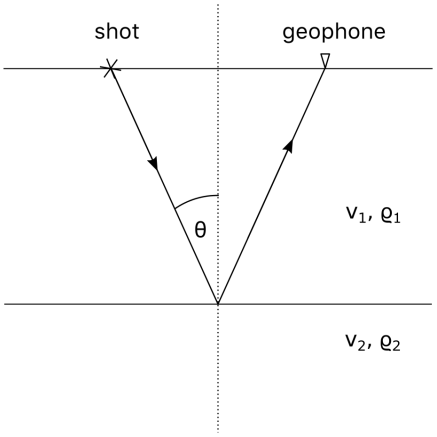

Figure 4.2: Ray path of a reflected wave in a layer-halfspace geometry.

signal at the TWTs of the reflected waves, the correlated signal displays maxima (and minima, respectively) at these times.
Using Eq. (4.14), the correlation of $y(t)$ with $s(t)$ yields

$$y'(t) = k(t) * \tilde{w}(t) * e(t) \tag{4.15}$$

(Yilmaz, 2001). $k(t)$ denotes the Klauder wavelet which is the autocorrelation of $s(t)$ (Yilmaz, 2001) and corresponds to the wavelet equivalent of an impulsive source generating the same record (Dobrin and Savit, 1988).
Initially, $k(t)$ is zero-phase, that is, being an autocorrelation, symmetric, and $\tilde{w}(t)$ is assumed to be minimum-phase. Hence, $k(t) * \tilde{w}(t)$ is mixed-phase which is inconsistent with the minimum-phase assumption of spiking deconvolution (section 4.3.2). However, after converting $k(t)$ into its minimum-phase equivalent, the processing steps discussed in section 4.3.2 can be applied to the vibroseis data similarly as to explosive source data.

4.3.4 The Reflection Coefficient and Velocity Terms

In this section, the reflection coefficient R and various velocity terms v are introduced. As only seismic P-wave data is considered in the current thesis, all following definitions refer to seismic P-waves.

Reflection seismics considers the signal from reflections of seismic energy at layer boundaries that are characterized by impedance contrasts. The seismic impedance Z_i of a layer i is calculated by:

$$Z_i = v_i \cdot \rho_i \tag{4.16}$$

(Yilmaz, 2001), with the seismic P-wave velocity v_i and the material's density ρ_i of that layer.

Figure 4.2 shows the ray path of a seismic wave reflected at a layer-halfspace boundary. The impedance of the above layer is $v_1\rho_1$, the impedance of the below halfspace

is $v_2\rho_2$. The angle of incidence is denoted by θ.
The reflection coefficient R for normal incidence (i.e. $\theta = 0°$) associated with the layer boundary, which is depicted in Fig. 4.2, is calculated from the two materials' seismic impedances:

$$R = \frac{v_2\rho_2 - v_1\rho_1}{v_2\rho_2 + v_1\rho_1} \ . \tag{4.17}$$

For incidence angles $\theta \neq 0°$, the Zoeppritz equations have to be considered. They provide a funcional relation between P- and S-wave velocities and the densities of the two materials, the incidence angle and the resulting reflection coefficient. The web site CREWES (2005) provides an interactive possibility to get R plotted against θ. However, for small values of θ, Eq. (4.17) is used as an approximation to compute R, which is done by assuming a small spread.

If the reflection coefficient is positive, the onset of the reflected wave appears also positive in the seismogram. If R is negative (i.e. the impedance contrast is negative), the seismic wavelet becomes 180° phase shifted at the appurtenant layer boundary, and thus, it appears negative in the seismogram. From this it follows that a material transition with a reflection coefficient of exactly 0 is invisible in seismic data. The Zoeppritz equations reveal that a reflector with $R = 0$ at normal incidence can appear in the seismic data with increasing angle of incidence, thus sometimes larger spreads are necessary to resolve reflectors in seismic data.

There are various velocity terms in seismic data processing: Regarding a horizontal and homogeneous layered stratigraphy, the interval velocity $v_{int,i}$ of a particular layer i denominates the seismic propagation velocity in this layer. In practice, since the layers aren't absolutely conform with these assumptions, $v_{int,i}$ denominates the average velocity in the i-th interval between two reflectors (Yilmaz, 2001).
The root-mean-square (rms) velocity $v_{rms,i}$ of the i-th layer is calculated as follows:

$$v_{rms,i} = \sqrt{\frac{\sum_{k=1}^{i} v_{int,k}^2 \Delta\tau_k}{\sum_{k=1}^{i} \Delta\tau_k}} \tag{4.18}$$

with the layers numbered from top to bottom. $\Delta\tau_k$ denotes the vertical TWT in the k-th layer.
The NMO velocity v_{nmo} is the velocity required to correct a seismic trace for NMO (see section 4.3.2).
In contrast, the stacking velocity v_{stk} is the velocity to get the best stacking result in a given CMP gather.

The traveltime equation of a wave reflected at the i-th layer boundary of a horizontal and homogeneous stratigraphy

$$t_i(x) = \sqrt{t_i^2(0) + \frac{x^2}{v_{rms,i}^2} + ...} \tag{4.19}$$

can be approximated under the assumption of a small spread with the hyperbola

$$t_{nmo,i}(x) = \sqrt{t_i^2(0) + \frac{x^2}{v_{rms,i}^2}} \tag{4.20}$$

or, to fit $t_i(x)$ in Eq. (4.19) best over the complete spread length, with the hyperbola

$$t_{stk,i}(x) = \sqrt{t_{stk}^2(0) + \frac{x^2}{v_{stk,i}^2}} \ . \tag{4.21}$$

Eq. (4.20) is the simplest model used to align the traces in a CMP gather so that the onsets of the reflected waves appear at their zero-offset TWT $t_i(0)$. Because the deviation between $t_{nmo,i}$ and t_i increases with larger values of x, the stacking velocity v_{stk} is used for offset correction in practice by which the reflection becomes aligned at $t_{stk,i}(0)$ and which yields the best possible stacking result.

4.3.5 Deriving Interval Velocities with Dix' Method

The Dix method enables to derive seismic interval velocities v_{int} from the travel time curve $t(x)$ of reflected waves. It is described in Dix (1955).
For a horizontal homogeneous layered substratum, the TWT $t_i(x)$ at offset x of the wave reflected at the i-th layer boundary is approximately given by

$$t_i(x) = \sqrt{t_i^2(0) + \frac{1}{v_{rms,i}^2}x^2} \tag{4.22}$$

(compare Eq. (4.20)). In this hyperbolic equation, $t_i(0)$ is the zero-offset TWT $t_i(x = 0)$ and $v_{rms,i}$ denotes the rms velocity of the i-th layer.
With $i > 1$, Eq. (4.22) is only an approximation which gives $t_i(x)$ if the raypath were a straight line and not the minimum time path which is given by Snellius' law. Plotting t_i^2 against x^2, v_{rms} can be calculated from the slope A of the regression line

$$t_i^2(x) = t_i^2(0) + A_i x^2 \tag{4.23}$$

by

$$v_{rms,i} = \frac{1}{\sqrt{A_i}} \ . \tag{4.24}$$

The interval velocity $v_{int,i}$ of the i-th layer can then be calculated from the relation

$$v_{int,i} = \sqrt{\frac{v_{rms,i}^2 \ t_i(0) - v_{rms,i-1}^2 \ t_{i-1}(0)}{t_i(0) - t_{i-1}(0)}} \ . \tag{4.25}$$

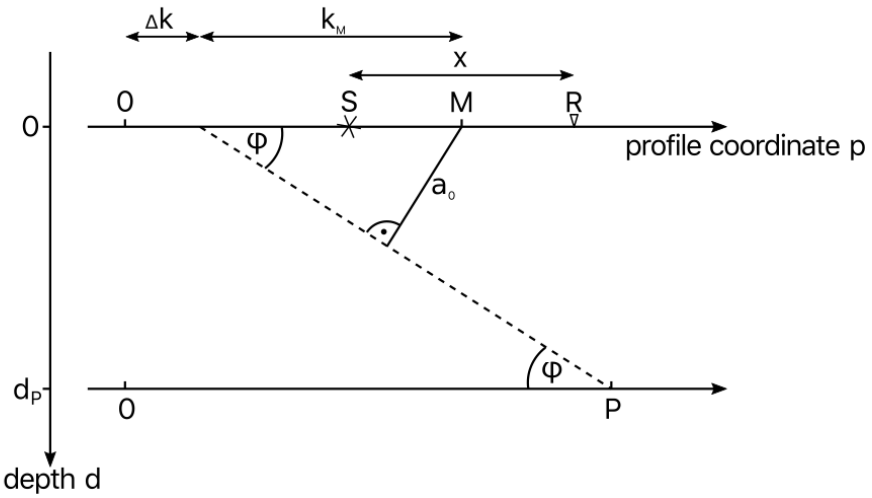

Figure 4.3: Geometry corresponding to the derivation of the offset-dependant TWT $t_{0,1}$ in the case of a dipping reflector. The capital letters S, R, M and P denote the profile coordinates p of the shot point, the receiver, their midpoint and a certain point on the reflecting plane whose depth is d_P, respectively.

4.3.6 Dip Correction of Dix' Method

The velocity determination with Dix' Method in the horizontal layered case as introduced in the previous section 4.3.5 is described in Dix (1955). For the case of a layer boundary dipping with φ, Dix (1955) further gives the linear equation

$$t_1^2(x) = t_{0,1}^2 + \frac{\cos^2\varphi}{v_{int,1}^2} x^2 \tag{4.26}$$

with which the interval velocity $v_{int,1}$ of the topmost layer can be derived. In the experiment geometry mentioned in Dix (1955), the zero-offset TWT $t_{0,1}$ in Eq. (4.26) is a constant due to the symmetrical motion of the shot and the receiver, the midpoint of which remains at a constant position.

As in the framework of the following data processing, the travel time equation $t_1(x)$ in the same dip case but with a different survey geometry is needed, it is derived according to Fig. 4.3. The geometry now consists of one stationary shot at the profile coordinate $p = S$ and many receivers at several coordinates $p = R$, so that $t_{0,1}$ in Eq. (4.26) becomes offset-dependent. In Fig. 4.3, the dashed line represents the dipped layer boundary, φ is the dip angle and a_0 denotes the length of the one-way ray path of the reflected wave with S and R both located at their midpoint M (which varies with moving receiver locations R).
The zero-offset TWT $t_{0,1}$ is given by

$$t_{0,1} = 2\frac{a_0}{v_{int,1}} \tag{4.27}$$

with the one-way travel path

$$a_0 = \sin\varphi \; k_M = \sin\varphi \; (M - \Delta k) = \sin\varphi \left(M - \left[P - \frac{d_P}{\tan\varphi} \right] \right) \tag{4.28}$$

where P is an arbitrary point on the reflector interface and d_P its depth, as seen in Fig. 4.3.
M can also be expressed by

$$M = S + \frac{1}{2}x \tag{4.29}$$

so that

$$a_0 = \sin\varphi \left(S + \frac{1}{2}x - [P - \frac{d_P}{\tan\varphi}] \right) \; . \tag{4.30}$$

Inserting Eq. (4.30) and Eq. (4.27) in Eq. (4.26) yields

$$\begin{aligned} t_1(x)^2 &= \left(2\frac{a_0}{v_{int,1}} \right)^2 + \frac{\cos^2\varphi}{v_{int,1}^2} x^2 \\ &= \frac{4}{v_{int,1}^2} \sin^2\varphi \left(S + \frac{1}{2}x - P + \frac{d_P}{\tan\varphi} \right)^2 + \frac{\cos^2\varphi}{v_{int,1}^2} x^2 \; . \end{aligned} \tag{4.31}$$

As the aim is to derive the dependency between t_1 and x, $u = S - P + \frac{d}{\tan\varphi}$ is used as the abbreviation for the constant part of the bracket in Eq. (4.31). In the following steps, Eq. (4.31) is simplified:

$$\begin{aligned} t_1^2(x) &= \frac{4}{v_{int,1}^2} \sin^2\varphi \; (u + \frac{1}{2}x)^2 + \frac{\cos^2\varphi}{v_{int,1}^2} \; x^2 \\ &= \frac{4}{v_{int,1}^2} \sin^2\varphi \; (u^2 + ux + \frac{1}{4}x^2) + \frac{\cos^2\varphi}{v_{int,1}^2} \; x^2 \\ &= \frac{4}{v_{int,1}^2} \sin^2\varphi \; u^2 + \frac{4}{v_{int,1}^2} \sin^2\varphi \; u \; x + \frac{\sin^2\varphi}{v_{int,1}^2} \; x^2 + \frac{\cos^2\varphi}{v_{int,1}^2} \; x^2 \\ &= \frac{4}{v_{int,1}^2} \sin^2\varphi \; u^2 + \frac{4}{v_{int,1}^2} \sin^2\varphi \; u \; x + \frac{x^2}{v_{int,1}^2} \\ &= \frac{4}{v_{int,1}^2} \sin^2\varphi \; u^2 + \left(\frac{x}{v_{int,1}} + \frac{2}{v_{int,1}} \sin^2\varphi \; u \right)^2 - \frac{4}{v_{int,1}^2} \sin^4\varphi \; u^2 \; . \end{aligned} \tag{4.32}$$

So the sought for linear equation is

$$t_1^2(x) = \frac{1}{v_{int,1}^2} \left(x + 2\sin^2\varphi u \right)^2 + \kappa \tag{4.33}$$

with the constant $\kappa = \frac{4}{v_{int,1}^2} \sin^2\varphi \; u^2 \cos^2\varphi$ which is independent of the offset x.

With the result given by Eq. (4.33), $v_{int,1}$ can be determined as the line slope if t_1^2 is plotted against $x'^2 = \left(x + 2\sin^2\varphi u \right)^2$. A disadvantage of this method, compared with the method derived by Dix (1955) where Eq. (4.26) can be used, is the

necessity of the layer depth d_P at some point P which requires additional information.

5 Experiment set-up

5.1 Experiment Parameters

The considered seismic data were recorded between May 9th and 20th, 2014, on Russell Glacier in Greenland as seen in Fig. 3.2. The experiment was performed by the glaciology group from the Alfred Wegener Institute.
In this thesis, seismograms from five different datasets are used to derive geological properties of the experiment location subsurface. The datasets are named 582, 511, 531, 522 and 532.

Table 5.1 gives a general overview of the line parameters while Fig. 5.1 shows the relative geometry of source and receiver locations of all five datasets.

For the vibroseismic line 582, the ELVIS III P-wave minivibrator generating 10 s sweeps with frequencies increasing linearly from 30 to 240 Hz was used as a source. For the explosive seismic lines 511, 531, 522 and 532, 250 g of dynamite were fired in 2 m deep boreholes. In all datasets, a 300 m long snow streamer with 96 channels (ch), resulting in a receiver spacing of $\Delta x = 3.125$ m, was used. Each geophone consists of a gimballed 30 Hz P-wave geophone. A spurious frequency of the geophones is 540 Hz.
The sample rate Δt amounts to 0.5 ms, so according to the Nyquist criteria, a maximal frequency of $f_{max} = \frac{1}{2\Delta t} = 1$ kHz can be resolved. The recording time of the explosive lines amounts to 3 s, for the vibroseis line 582, it is 13 s because of the temporal extent of the signal.
To georeference the experiment, the absolute coordinates were determined with handheld GPS. For the seismic processing software, UTM coordinates were generated.

The profiling lines 582, 511 and 522 have a constant relative geometry between the source and the receiver, in order to cover a long one-dimensional area in the subsurface evenly as shown in Fig. 5.2. The shot spacing is chosen as 75 m which

Line Name	Source	Type	number of SP	direction	direction of recording
582	ELVIS III	profiling	26	257°	east to west
511	explosives	profiling	62	257°	east to west
531	explosives	CMP	6	257°	east to west
522	explosives	profiling	13	347°	south to north
532	explosives	CMP	3	347°	north to south

Table 5.1: Overview of the seismic line parameters.

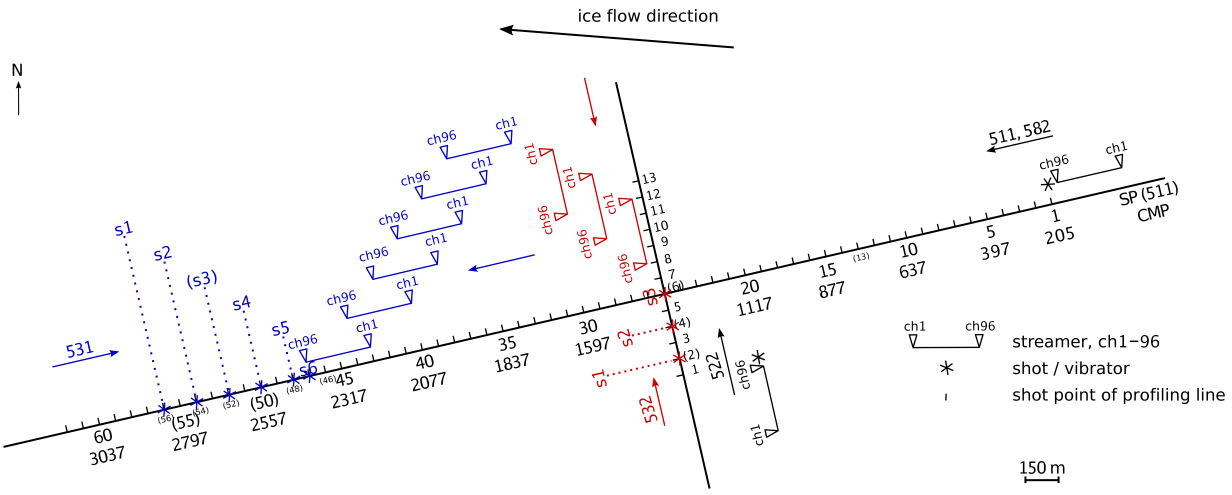

Figure 5.1: Relative geometry of the 5 different seismic lines 582, 511, 531, 522 and 532. The lines 582, 511 and 522 are profiling lines, i.e. the relative geometry of the shot and the streamer remains constant and is moved along the respective line. With the CMP lines 531 and 532, the shots and the streamer positions are moved towards each other, covering larger offset ranges.
Bracketed shot point numbers denote missing data.

will be explained in the following section 5.2.
While processing the seismic data, a "small-spread assumption" is used. Thereby, the angle between the seismic ray and the vertical is neglected in several processing steps. According to this assumption, the maximal offset has to be less than the target depth. At the same time, larger offsets favor the data quality in reflection seismics, because the direct wave then becomes less dominant in the data due to geometrical spreading. As a compromise, the offset between shot point (SP) and the 96-th geophone is chosen as the septuple of the geophone spacing, which is $7 \cdot \Delta x = 21.875\,\mathrm{m}$.

Figure 5.1 illustrates the relative geometry of SP and streamer positions of all five seismic lines.
Line 511 is the main line of the survey and comprises of 62 SPs, i.e. it is $61 \cdot 75 = 4575\,\mathrm{m}$ long. It was recorded from east to west in 257° direction, which is approximately parallel to the ice flow described in section 3.2.2.
The sweep locations of line 582 are the 26 easterly SPs of line 511, i.e. SP1 to SP26. From SP18 to SP26, 5 sweeps were recorded per sweep location and from SP1 to SP17, there was 1 sweep per SP.
Line 522 crosses the main line 511 at SP25, which equals SP6 of line 522, as visible in Fig. 5.1. It runs from south to north in the 347° direction and consists of 13 shot locations.

Lines 531 and 532 are CMP lines, i.e. source and receiver are moved towards each other covering the same CMP area, thereby covering a large offset range.
The acquisition geometry of 531 and 532 is shown in Fig. 5.1 in blue and red, respectively. For the sake of clarity, the shot (s) and channel locations are shown parallel shifted to the lines of 511 and 522 on which they lie. The offset range of 531 runs from minimally 0 m (which is between s6 and ch96) to 1797 m (s1, ch1). The offset

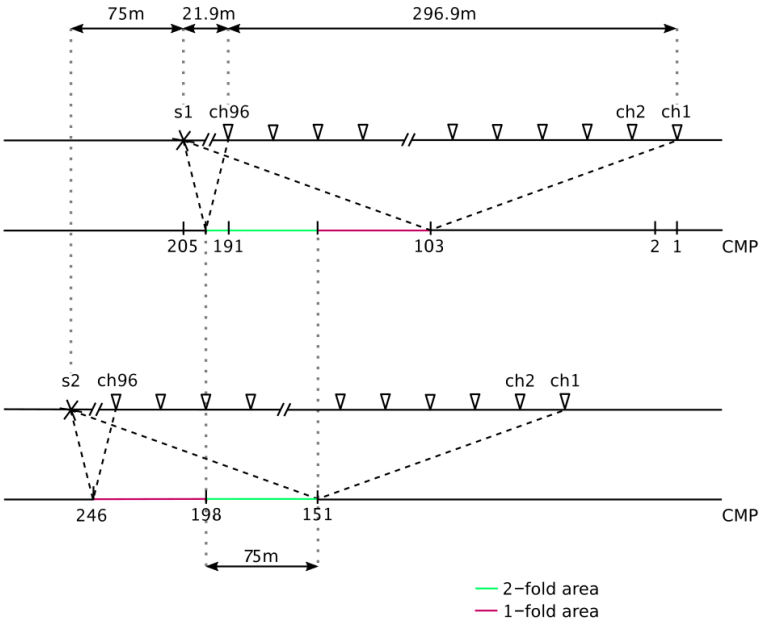

Figure 5.2: CMP coverage for the geometry of the profiling lines 582, 511 and 522. The SP spacing of 75 m yields a 2-fold coverage of the green-colored reflector area. As SP18 to 26 were each recorded five times with the vibroseis data, there is a 10-fold coverage in the associated area.

range of 532 is from 150 m to 1047 m.
The six shot locations of line 531 coincide with SP47, 48, 50, 52, 54 and 56 of line 511. The shots run from west to east while ch96 of the streamer was moved from SP36 westward up to SP47 of line 511.
Line 532 consists of three shots s1, s2 and s3, which are located at SP2, 4 and 6 of the profiling line 522. The acquisition took place with the shots running from south to north while the streamer was moved from north to south, ch96 moved from 522's SP12 over SP10 to SP8.

As depicted in Fig. 5.1, the streamer is located on the eastern side of the particular shot with the lines 582, 511 and 531. For line 522, the streamer lies in the south, for line 532 in the north of the associated shot location.

5.2 Common-Midpoint Coverage

In this section, the coverage of the reflection area beneath the survey lines introduced in the previous section 5.1 is considered, assuming horizontal stratigraphy. As explained in section 4.3.2, the reflection points on a flat reflector lie vertically below the source-receiver midpoints. That is why the reflection points associated with seismic traces which have the same source-receiver midpoint (i.e. the same CMP) are called CDPs (Common Depth Points).

Figure 5.2 depicts the relative geometry of the profiling lines 582, 511 and 522 including the ray path range for a horizontal reflector.

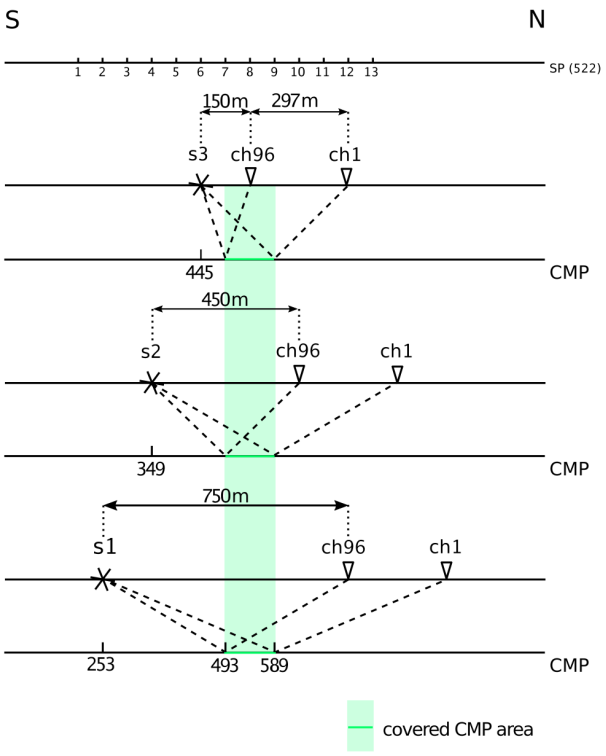

Figure 5.3: Geometry of the CMP line 532 in the case of a horizontal reflector, including the CMP numbers from the 522 geometry. The 150 m long CMP range from CMP 493 to 589 is covered 3-fold.

The CMP spacing results from the receiver spacing as $\Delta c = \frac{\Delta x}{2} = 1.5625\,\text{m}$ (because of its submillimeter accuracy, this value suits only theoretical purposes). The location of CMP number 1 is defined as directly below the far-offset ch1 of SP1, i.e. at the beginning of the line, see Fig. 5.2. At lines 582 and 511, this is at the eastern and at line 522 at the southern line end. The CMP numbering of the CMP lines 531 and 532 equals to that of the profiling lines, i.e. the CMP numbers remain at their place on each of the two perpendicular profiles.
In the geometry of the profiling lines shown in Fig. 5.2, the first covered CMP is located in the center between SP1 and the corresponding ch1 and for this reason it has the number 103. Besides, the location of the first shot point coincides with CMP 205. It is visible that with the chosen SP interval of 75 m and the streamer length of 300 m, 2-fold seismic data is achieved.

Thus, the 511 dataset is 2-fold, with the following exceptions: As the shots on SP13, 46, 48, 50, 52, 54, 55 and 56 of line 511 were not recorded (among them, SP48, 50, 52, 54 and 56 that were used for the CMP line 531, as visible in Fig. 5.1), there is a 148 m long coverage gap between CMP 2695 and CMP 2790 and only 1-fold coverage in the CMP intervals 679-774, 2263-2694 and 2791-2838.
Because SP2, 4, and 6 of the crossline are used for the CMP line 532, the 522 dataset is 1-fold between CMP 151-438, i.e. in the south of the crosspoint with line 511, which is at CMP 445 of line 522 and at CMP 1357 of line 511, respectively. In the north of the crosspoint, the 522 data is 2-fold.
Only with the vibroseismic line 582 and there from SP18 to SP26, 5 sweeps were performed at each SP, making that dataset 2-fold $\cdot$ 5 = 10-fold.

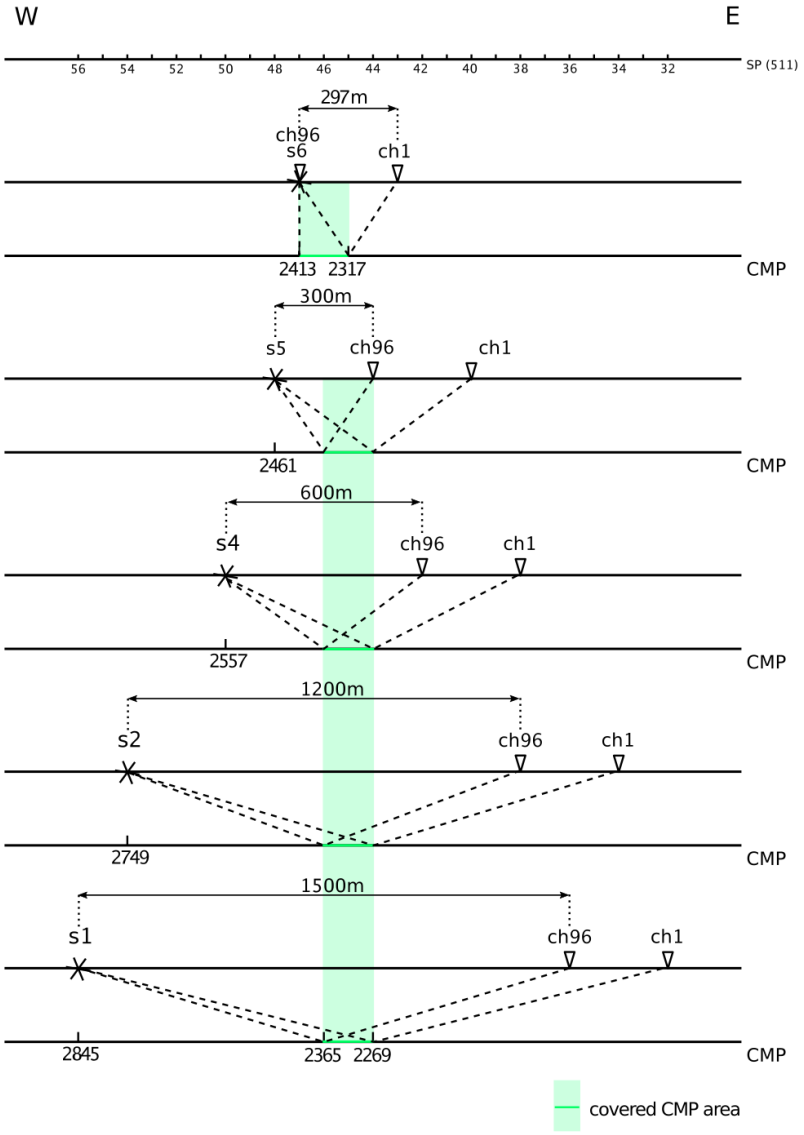

Figure 5.4: Geometry of the CMP line 531 in the case of a horizontal reflector, including the CMP numbers from the 511 geometry.

Figure 5.3 illustrates the reflector coverage of the CMP line 532 for a flat reflector. With all three shots, the same CMP area from CMP 493 to 589 (line 522) is covered.
The construction of the CMP coverage of 531 is displayed in Fig. 5.4. The dataset is 4-fold from CMP 2269 to CDP 2316, 5-fold from CMP 2317 to 2365 and 1-fold from CMP 2366 to 2413 due to the locations of the five shots s1, s2, s4, s5 and s6 that were recorded.

6 Data Processing

To process the seismic data from the different lines depicted in Fig. 5.1, the seismic reflection processing software Paradigm EPOS 2011.3 is used.
The theoretical background of the processing steps applied in the following sections 6.1 and 6.2 is introduced in section 4.3.
Since the raw field data are in seg2 format, they are first converted into the software-specific disco format (.dsk).

6.1 Data Processing of the Vibroseismic Dataset 582

The 13 s long vibroseis data from line 582 are first correlated with a 10 s synthetic sweep as the vibrator source signal has not been recorded in the field. The correlation reduces the data length to 3 s which equals the recording length of the explosive datasets.
As mentioned in section 5.2, five sweeps per location were recorded on SP18 to 26 and one sweep on SP1 to 17. Therefore, two separate but similar processing flows were created for the 582 data, one including 2-fold data from all source locations, with the best shot record chosen from each of the last shots; the other including the whole 10-fold dataset of SP18 to 26.

The correlated shot sections of both the 2-fold and the 10-fold dataset reveal the first arrivals of the direct wave, distinct reflections are not visible in that stage. The applied processing steps are listed in the following, a detailed description and illustration of the processing flow follows in the subsequent section 6.2 with the 511 data.

After the application of a 180° phase shift, static corrections in time were applied at the data of the shots 58 to 62, using the timing of the first arrivals of the direct wave. A trace editing to improve the signal-to-noise ratio follows, as well as the muting of the first arrivals by a manually applied muting filter. Then, the data is corrected for spherical divergence which will be explained more detailed in the following section 6.2. Finally, the traces are sorted by their CMP, then corrected for NMO and bandpass filtered. In contrast to the explosive dataset 511, where the source frequency content is not known, the sweep's frequency range from 30 to 240 Hz could be used for bandpass filtering in the processing of the vibroseis dataset 582. After all, the data is stacked, which results in the stacked sections shown in the Figs. 6.1 and 6.2.

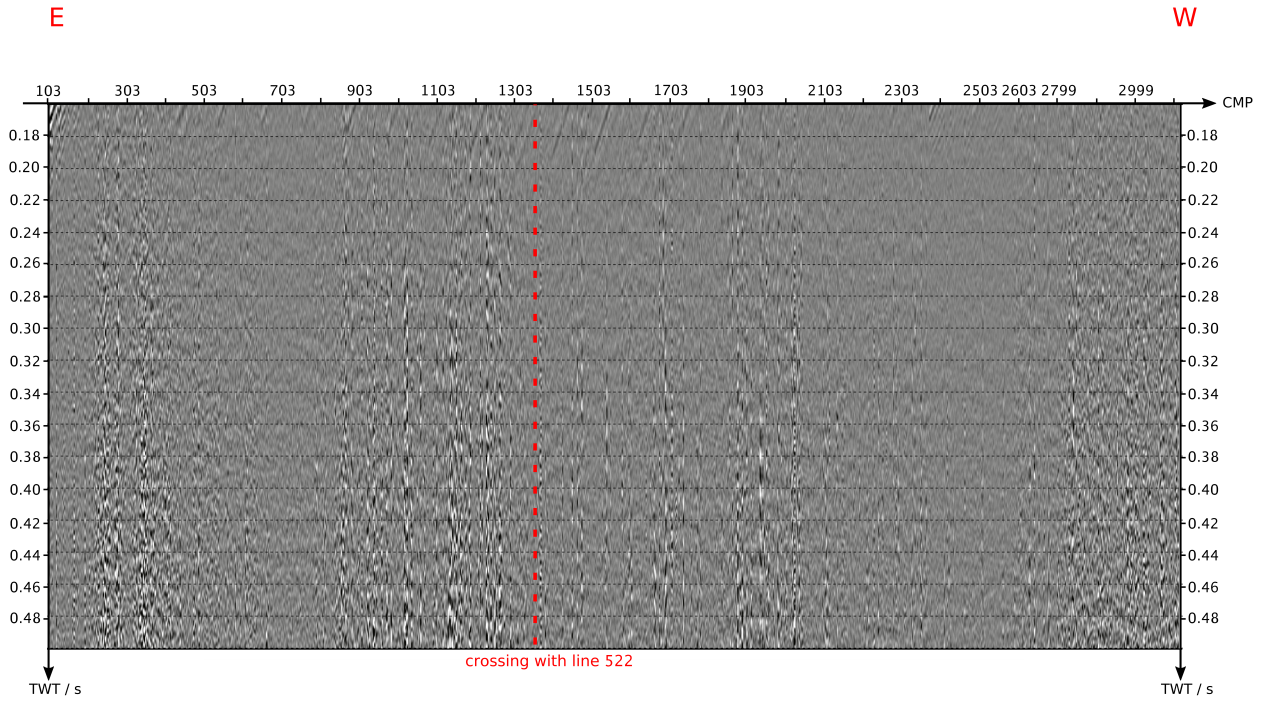

Figure 6.1: Stacked section of the 2-fold vibroseis data from line 582.

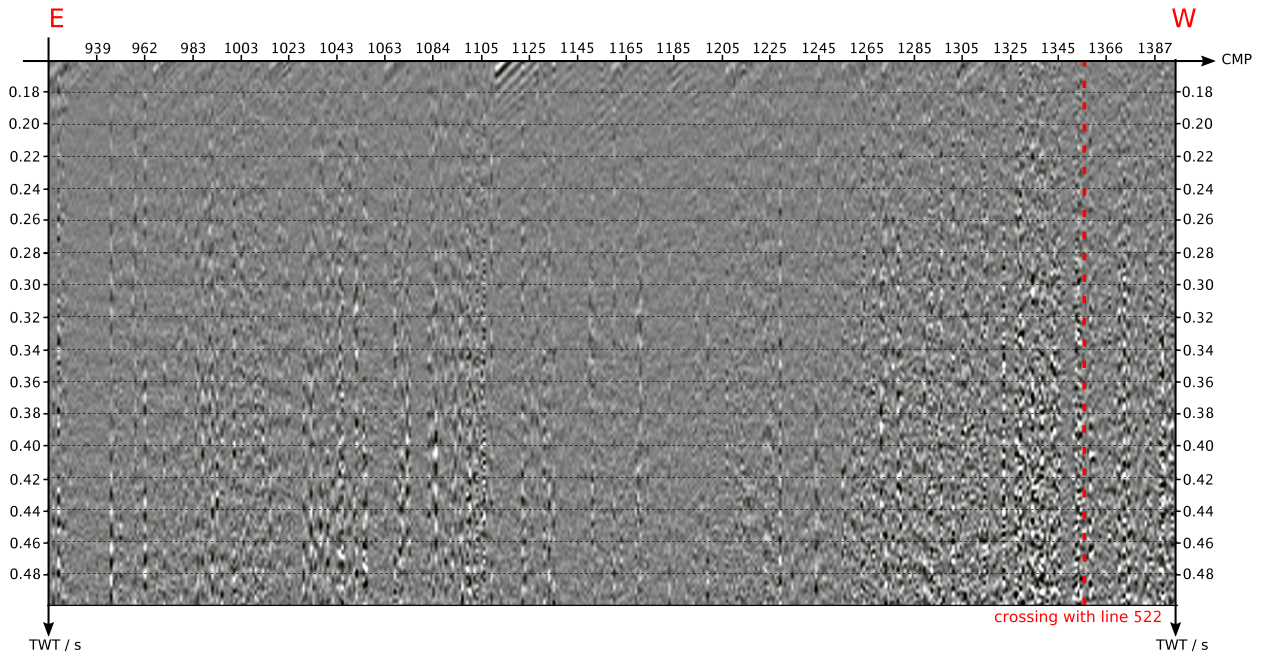

Figure 6.2: Stacked section of the 10-fold vibroseis data from line 582. Five sweeps were recorded on each of the last nine SP of 582, i.e. SP 18 to 26 of line 511.

6.2 Data Processing of the Profiling Lines 511 and 522

In the following, the data processing steps applied at the explosive seismic data from line 511 are described. The steps conducted at the other profiling datasets 522 and 582 correspond essentially to that description, however, not all methods were productive at all datasets, so these were then left out.

Phase shift:
In the framework of data preprocessing, a phase shift of 180° is applied to all traces. This is done because the data show negative first arrivals while they should be positive, as the source signal starts with a compression.

Trace editing:
Traces with a low signal-to-noise ratio are then omitted to improve the seismogram quality. Particularly the small-offset channels were skipped because of their higher noise amplitudes.
From the geometry of the profiling lines it follows that the channels 1 to 48 associated with a SPX are covering the same CMP range as the channels 49 to 96 of the previous SP$(X-1)$, horizontal stratigraphy assumed. This geometric characteristic is used to preserve a minimal one-fold coverage to not lose any covered CMPs in the resulting stacks.

Top mute:
After that, the direct waves' energy is muted by a manually applied topmuting.

Spherical divergence correction:
The amplitude decrease due to the spreading of the seismic energy as a spherical wave is incorporated with a spherical divergence correction. Only the first order effect, which is offset-independent, is taken into account by multiplying all traces with a time-dependent scalar.

Spiking deconvolution:
After the described preprocessing steps (phase shift, trace editing, top mute, spherical divergence correction), spiking deconvolution is applied to the seismic data. For pre-whitening, 0.2 % of white noise is added to the data. As explained in section 4.3.2, the deconvolution filter is designed using a time window around the reflection visible in the data. The operator length is chosen as 25 ms which is the half of the design window's length which goes from $t = 350$ s to 400 s. The deconvolution filter is then applied from $t = 250$ ms to 500 ms. As visible in Fig. 6.3, spiking deconvolution sharpens the reflection onset in the data.

After deconvolution, some more filters are applied to the data to further improve the signal-to-noise ratio.

f-k filtering: Figure 6.4 shows on the left the first shot record of line 511 (after deconvolution is applied) in ch-TWT coordinates and on the right its amplitude

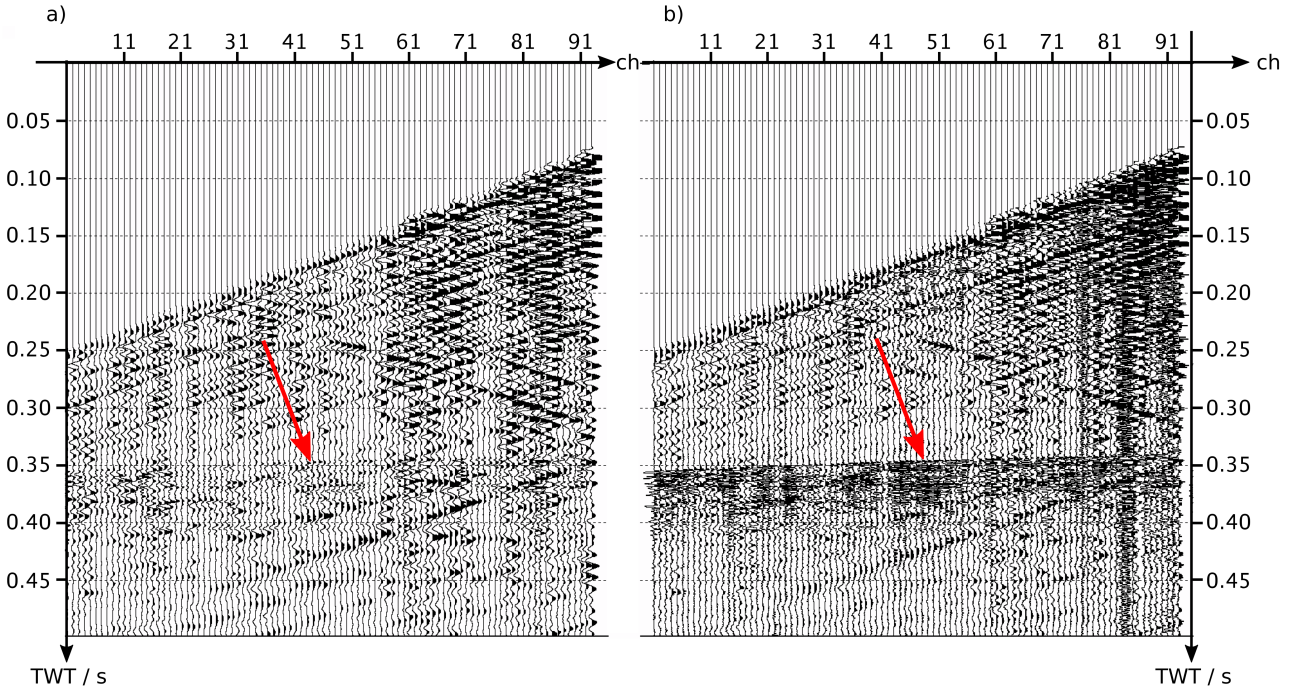

Figure 6.3: Shot record 1 of line 511 a) before and b) after spiking deconvolution. The red arrows indicate the reflection horizon which becomes more distinct in b).

spectrum after a 2-D Fourier Transform. The thin red line in b) shows the chosen f-k filter, with its pass zone inside the triangle and its reject zone outside. The high-amplitude dipping energy in the f-k spectrum corresponds to the linear coherent noise visible in the seismogram, as denoted by the red arrows in both diagrams. Figure 6.5 shows the result of f-k filtering: The f-k filter has eliminated the coherent noise energy, but also induced noise which is particularly visible at early times. The latter mentioned effect is incorporated with a reapplication of the topmuting step which has been conducted during the above described preprocessing.

Bandpass filtering:
After that, the low and high frequency noise is rejected by the application of a bandpass filter. The filter has trapezoidal shape with the corner frequencies 5 Hz, 10 Hz, 500 Hz and 540 Hz, so the spectral components between 10 and 500 Hz are passed. Figure 6.6 shows the effect of the bandpass filter on the seismogram of shot 1, Fig. 6.7 the corresponding amplitude and phase spectra.
It is visible that especially the ringing of the small-offset traces marked with a red arrow in Fig. 6.6 could be suppressed by the bandpass filter. The corresponding frequency peak at approximately 540 Hz seen in Fig. 6.7 accords with the spurious noise frequency of the used geophones.

Sorting:
Before stacking the traces corresponding to the same CMP, the data is firstly sorted by CMP number to get CMP gathers from the initial shot gathers (these are, in contrast to CMP gathers, composed of seismic traces resulting from the same shot).

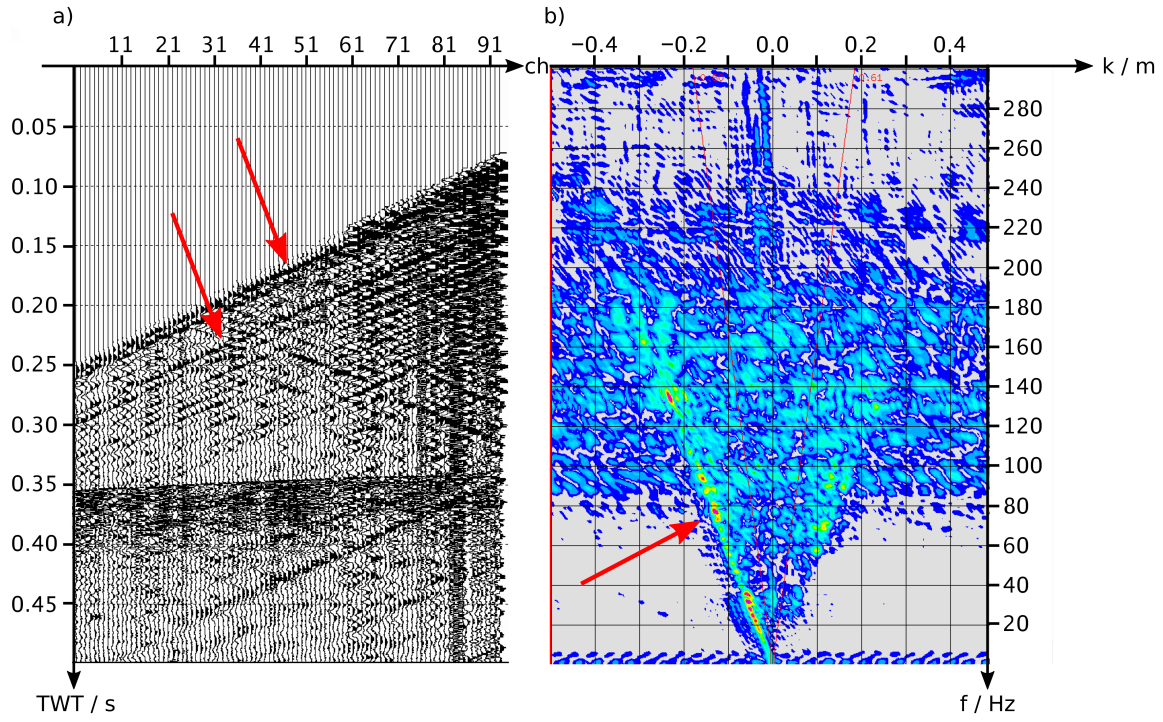

Figure 6.4: Shot record 1 of line 511 in a) the x-t domain and b) the f-k domain, before f-k-filtering. The red arrows are directed at the contained linear coherent noise, which appears as high-amplitude dipping event in the f-k spectrum.

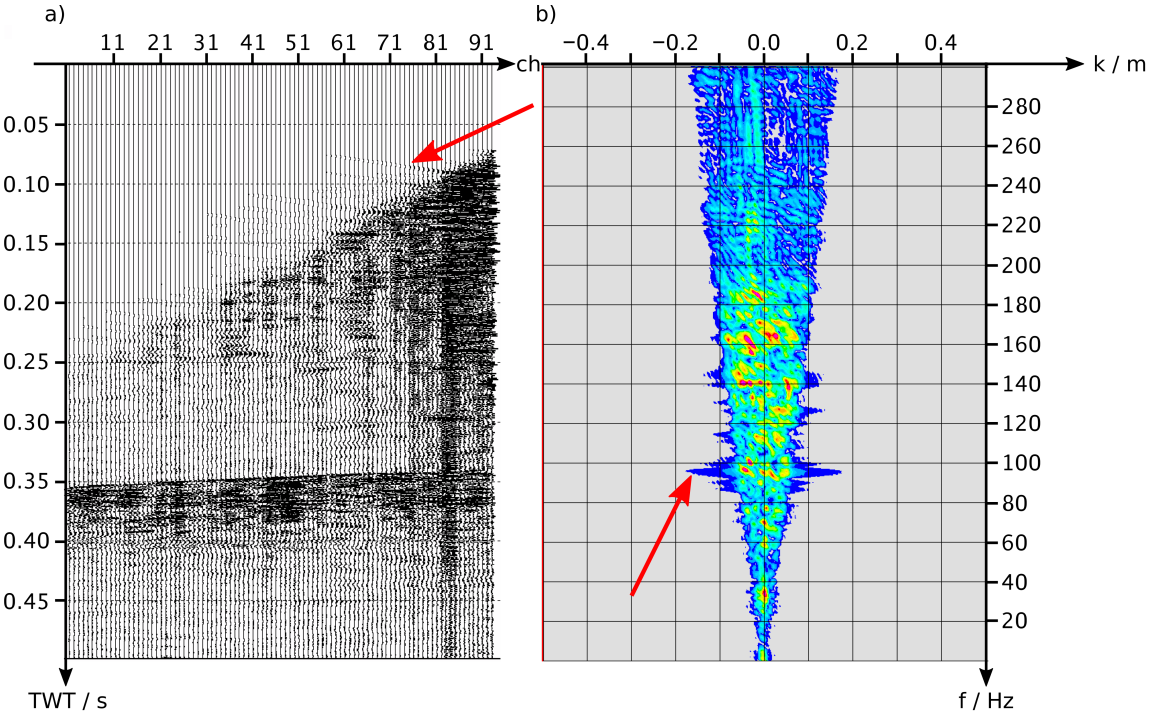

Figure 6.5: Shot record 1 of line 511 in a) the x-t and b) the f-k domain, after f-k-filtering. The red arrows point to the noise induced by the f-k filter.

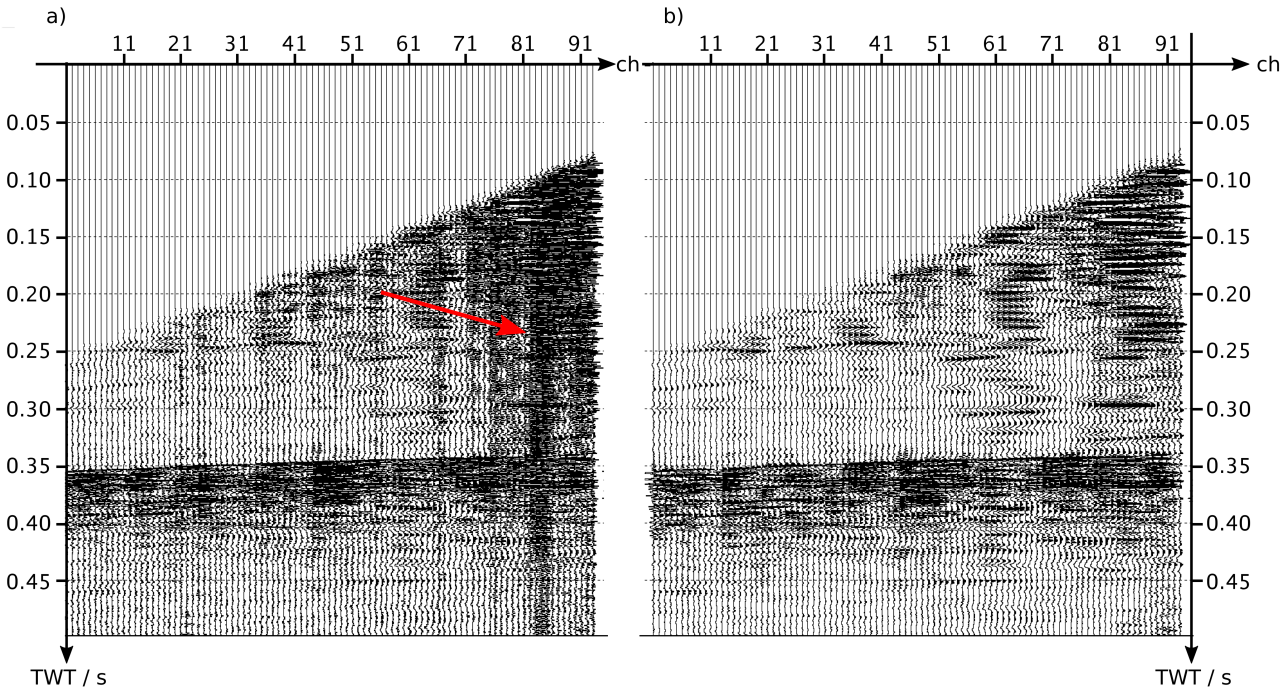

Figure 6.6: Shot record 1 of line 511 a) before and b) after the application of the trapezoidal bandpass filter, passing frequencies between 10 and 500 Hz. The red arrow indicates the ringing of the small-offset traces caused by spurious noise of the geophones at approx. 540 Hz which become suppressed by the filter.

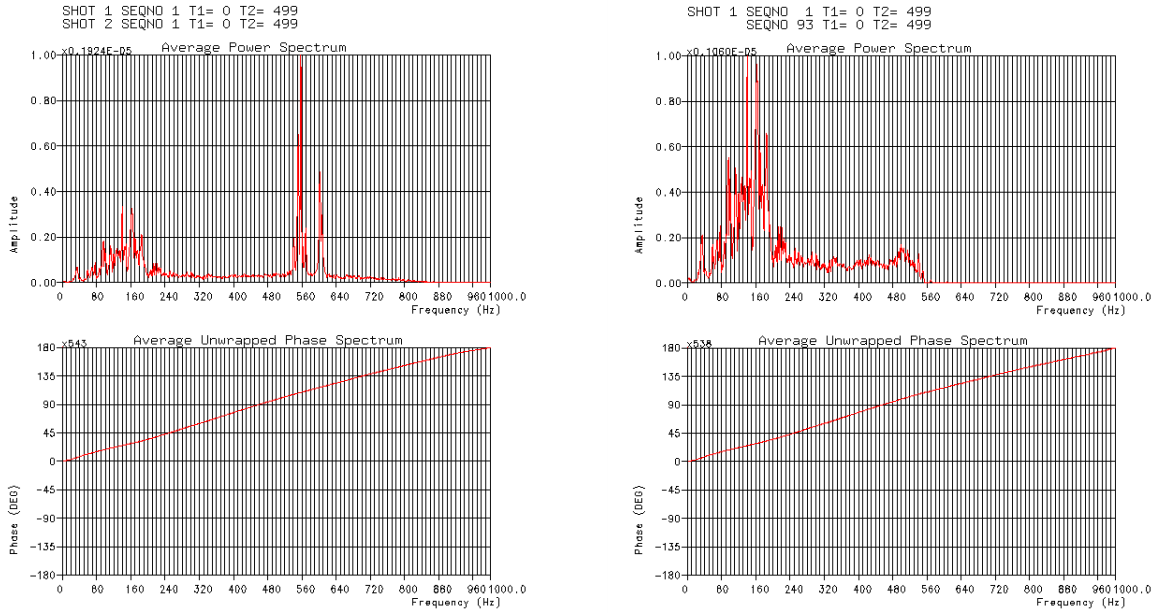

Figure 6.7: Amplitude and phase spectra corresponding to the seismogram of the first shot shown in Fig. 6.6 showing shot record 1 of line 511 before (left) and after (right) bandpass filtering.

NMO correction:
As introduced in section 4.3.2, the data then is corrected for normal moveout. Therefore, a stacking velocity model is used which the software generates from a manually specified interval velocity model. The development of the interval velocity model is precisely described in the sections 6.3 and 8.2. It includes information from the existing datasets as well as from previous knowledge of the glaciology and geology in the survey area.

Stacking and residual static corrections:
After the NMO correction, the stacking takes place. The resulting stacked section (stack) gives a preliminary image of the subsurface structure. The visible main reflection (approximately between TWT $t = 0.275\,\mathrm{s}$ and $0.345\,\mathrm{s}$) doesn't appear as a smooth horizon but includes abrupt jumps. These jumps occur between traces of adjacent shot gathers and result on the one hand from the surface topography and on the other hand from water content along the seismic ray path. A local higher elevation as well as the influence of water induce a delay of the reflected wave in the appropriate seismograms. As both of the effects aren't exactly known because of the inaccurate GPS elevation values and the unknown water distribution in the subsurface, static corrections in time are applied manually to the data. This is done by measuring the time jumps in the stack and shifting whole shot sections in time relative to each other so that the reflection energy from the different shot records becomes aligned in the stack. In order not to shift the whole dataset, which would represent an effective displacement of the recorded reflection in time, the static corrections are applied average-free so that the total time shift remains zero. The stack resulting with the static corrections applied before sorting and NMO correction is shown in Fig. 6.8. In Fig. 6.8, as well as in the following Figs. 6.9, 6.10 and 6.11, a CMP coordinate is specified. This variable denotes the distance in meters from CMP 1 of line 511 or 522. The crosspoint of 511 and 522 is depicted as dashed red line at CMP 1357 (in the case of line 511) or CMP 445 (line 522).
Figure 6.10 shows the stack of the 522 data.

Migration:
Finally, the stacked sections of the 511 and 522 data are time-migrated applying Omega-X Finite Difference Migration using a constant velocity model with a seismic interval velocity of the ice layer of $v = 3500\,\mathrm{m\,s^{-1}}$, which is determined in section 8.2. Figure 6.9 shows the result which represents the subsurface structure in CMP-time coordinates. To improve the quality of the migrated stack, the trace selection mentioned in the framework of preprocessing is optimized through omitting traces causing many 'smiles' in the migrated section.
After an equivalent processing applied at the 522 data, the migrated stack shown in Fig. 6.11 results.

6.3 Velocity Analysis with the CMP Lines 531 and 532

As mentioned in section 6.2, a seismic velocity model is required for the NMO correction of the data from the profiling lines 582, 511 and 522. On top of that, the

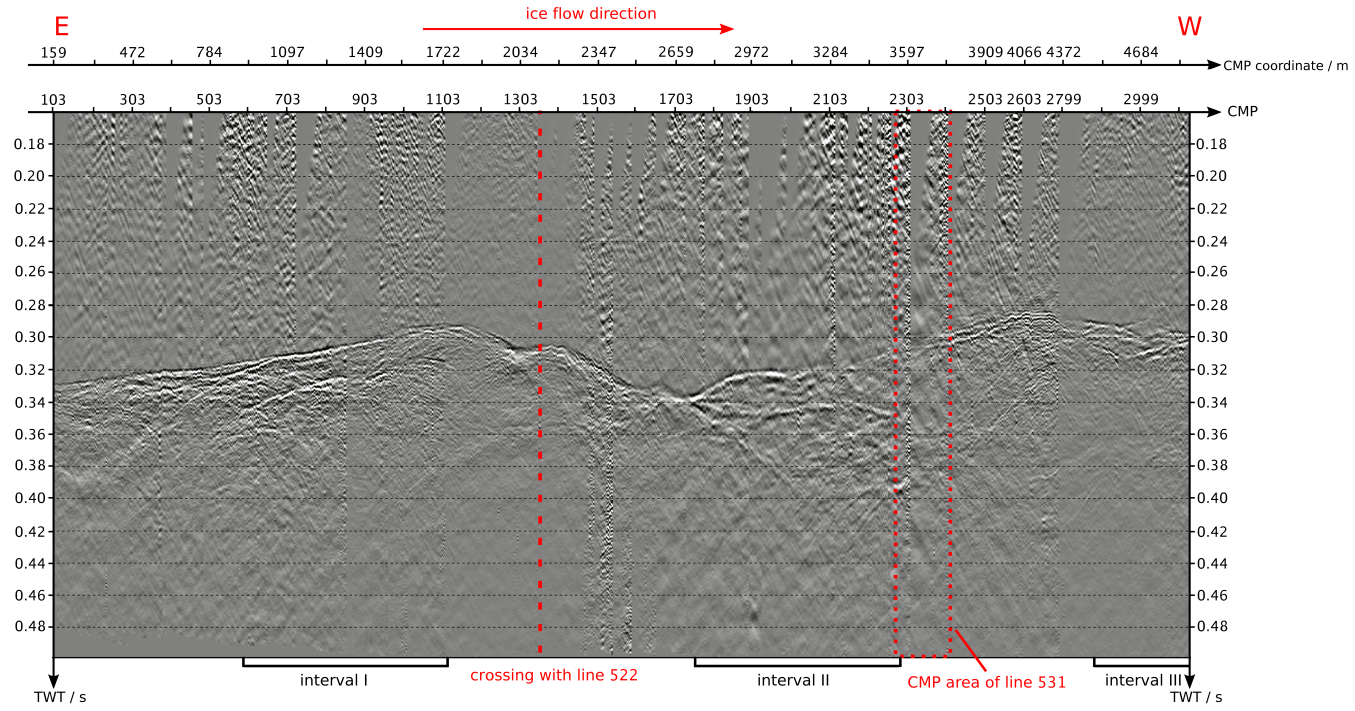

Figure 6.8: Stacked seismic data from line 511 with static corrections applied before sorting and NMO correction. The red dashed line designates the crosspoint with line 522 at CMP 1357. Also in red, the CMP area from CMP 2269 to CMP 2413 associated with the 531 dataset is marked. The three marked intervals I, II and III denote the areas where a second reflector is visible.

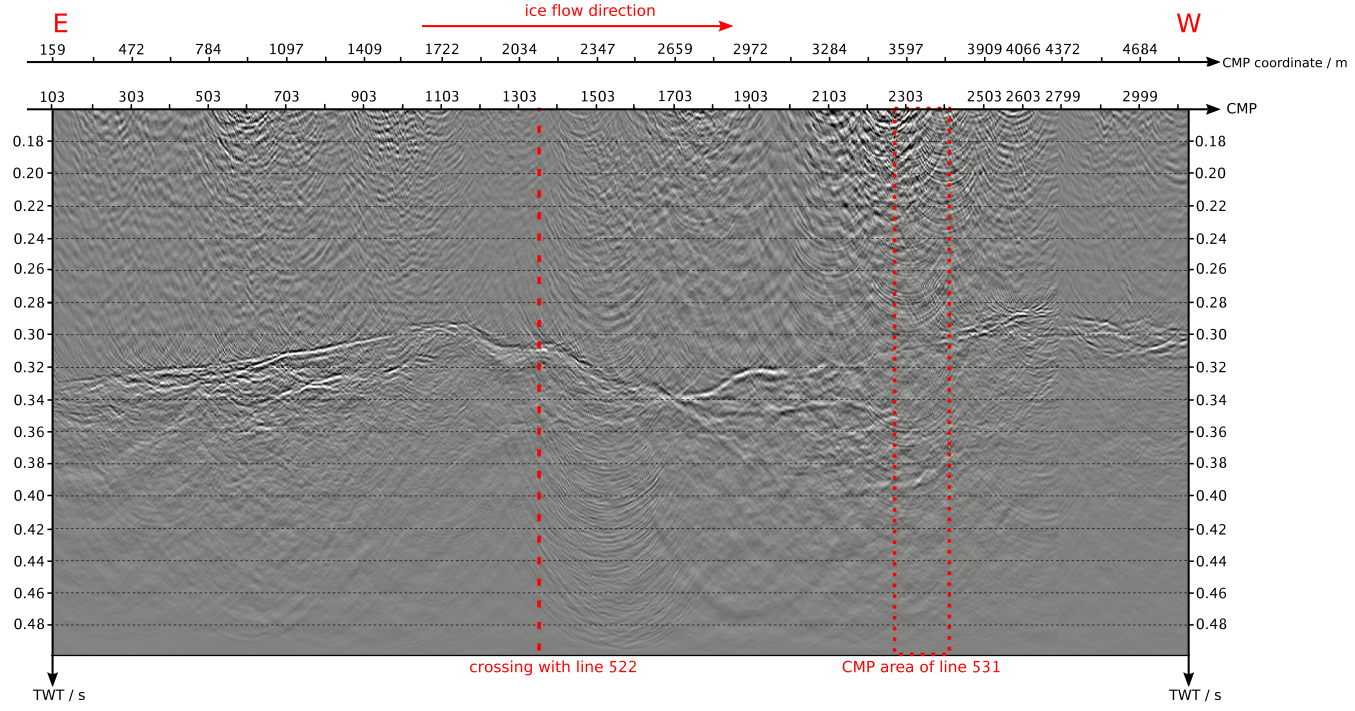

Figure 6.9: Migrated stack of line 511. The red dashed line designates the crosspoint with line 522 at CMP 1357. Also in red, the CMP area from CMP 2269 to CMP 2413 associated with the 531 dataset is marked.

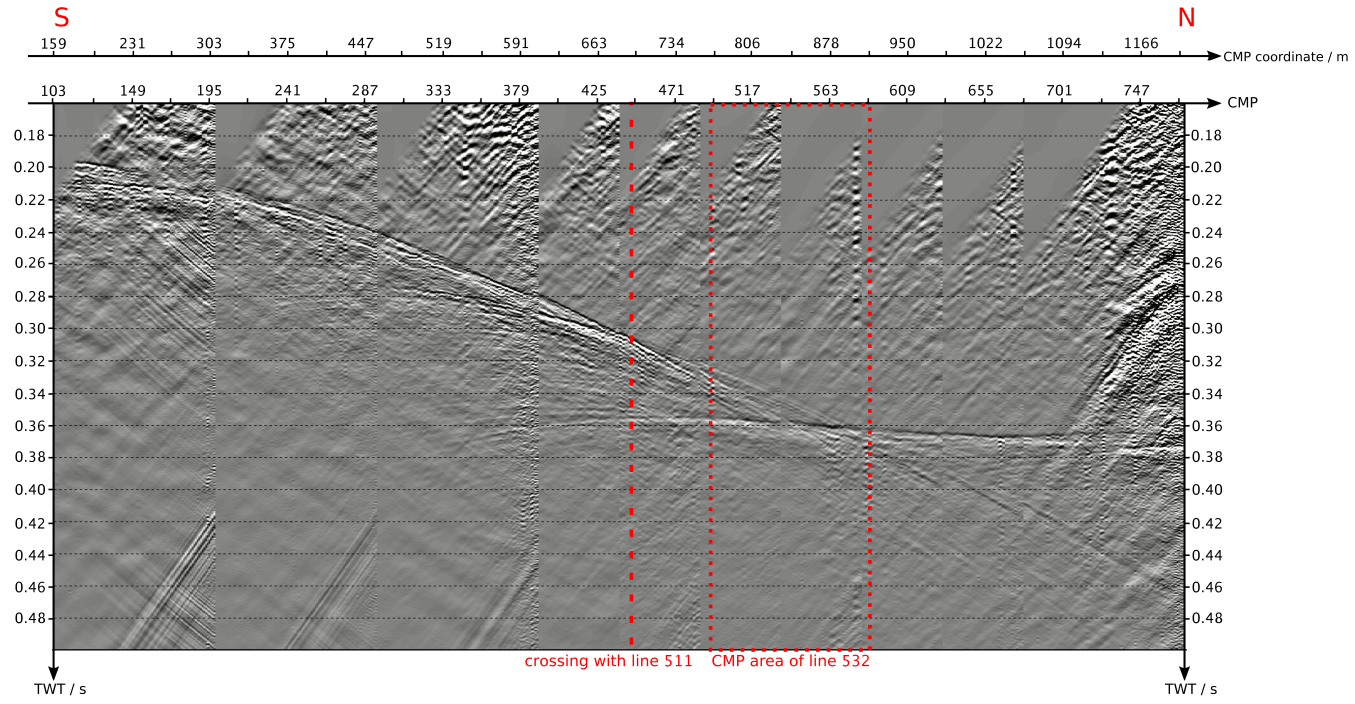

Figure 6.10: Stacked seismic data from line 522. The red dashed line designates the crosspoint with line 511 at CMP 445. Also in red, the CMP area from CMP 493 to CMP 589 associated with the 532 dataset is marked.

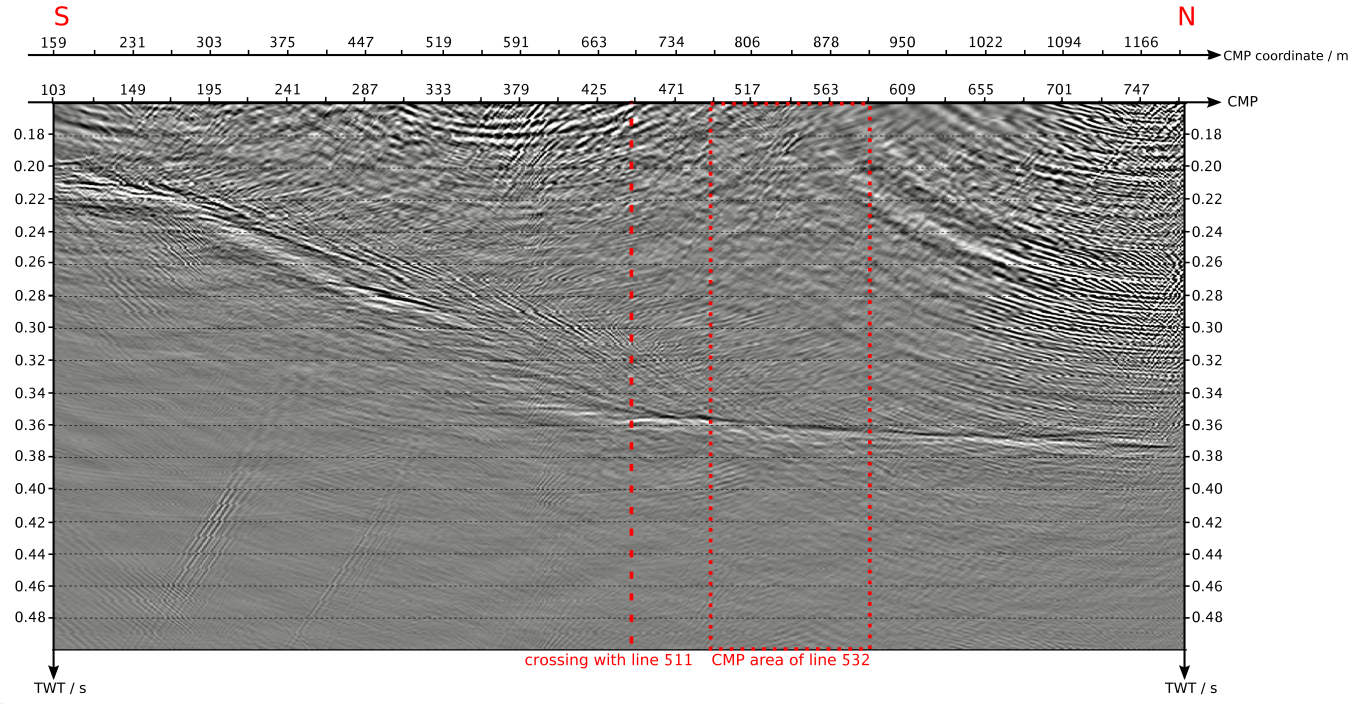

Figure 6.11: Migrated stack of line 522. The red dashed line designates the crosspoint with line 511 at CMP 445. Also in red, the CMP area from CMP 493 to CMP 589 associated with the 532 dataset is marked.

subsurface properties can be derived from the velocity values in the different layers. For these purposes, the seismic interval velocities of the subsurface are now determined by applying Dix' method (see section 4.3.5) on the CMP data 531 and 532, the offset of which extends over larger intervals than the offset of the profiling lines.

Before doing that, to have a first approximation of the seismic P-wave velocity in the glacier ice layer, the P-wave velocity in the near-surface ice is determined from the slope of the direct wave in the shot gathers, by dividing the offset difference Δx by the travel time difference Δt of the direct wave. This is done at both the 582 and the 511 dataset. From line 511, a velocity of

$$v = 3737\,\mathrm{m\,s^{-1}} \approx 3700\,\mathrm{m\,s^{-1}} =: v_{ice,surf} \tag{6.1}$$

results by averaging the values determined from the particular shot records. $v_{ice,surf}$ in Eq. (6.1) denotes the rounded result for the P-wave velocity in the near-surface ice layer.
In the 582 data, the determined values disperse strongly between $3200\,\mathrm{m\,s^{-1}}$ and $3800\,\mathrm{m\,s^{-1}}$. This is because the direct P-wave is only obvious at the near-source traces which are especially noisy so the picking of the time values was often not distinct.
The value $v_{ice,surf}$ given in the above Eq. (6.1) is in the following used as a reference value, when the seismic velocity value in ice is required indirectly, e.g. to determine the slope of the first reflector.

The Figs. 6.12 and 6.13 show the CMP data of the lines 531 and 532 in shot sections, both the 531 and 532 data deconvolved and the 531 data additionally bandpass-filtered. Both of the datasets reveal two reflection events, which are marked by red arrows with numbers 1 for the upper and 2 for the lower reflection. As in the shot sections of s2 and s4 in the 531 dataset, no distinct second reflector, but several coherent events are visible, two horizons are picked in each of them, denoted with 2,u for the upper and 2,l for the lower event.
To apply Dix' method at the data, as it is described in section 4.3.5, the offset x and TWT t of both reflection onsets 1 and 2 are picked in the shot gathers of 531 and 532.

After that, the CDP area covered by the CMP data 531 and 532 is determined with the help of the appurtenant reflector structure visible in the seismic stacks from the 511 and the 522 data. This is first of all done for the first event.
The CMP area of line 531 is marked in the migrated stack of line 511 displayed in Fig. 6.9, it runs from CMP 2269 to CMP 2413 of line 511. Respectively, the CMP area of line 532 running from CMP 493 to CMP 589 of line 522 is marked in the migrated stack of line 522 displayed in Fig. 6.11. The reflector's dip in both areas yields a displacement of the covered CDPs with respect to the CMPs.
The mean slopes φ_{531} and φ_{532} of the reflection areas of the 531- and the 532 data are determined from the unmigrated stacks of 511 and 522 (Figs. 6.8 and 6.10), using Eqs. (4.12) and (4.13). This approach is chosen due to the better resolution of the unmigrated stacks compared to the migrated stacks.
By inserting $v = v_{ice,surf}$, $\left(\frac{\Delta t}{\Delta x}\right)_{531} = \frac{26.5\,\mathrm{ms}}{584.375\,\mathrm{m}}$ and $\left(\frac{\Delta t}{\Delta x}\right)_{532} = \frac{40.5\,\mathrm{ms}}{148.4375\,\mathrm{m}}$, respectively, in Eq. (4.12) and the resulting values for $\frac{\Delta \tau}{\Delta x}$ in Eq. (4.13), the sought for angles

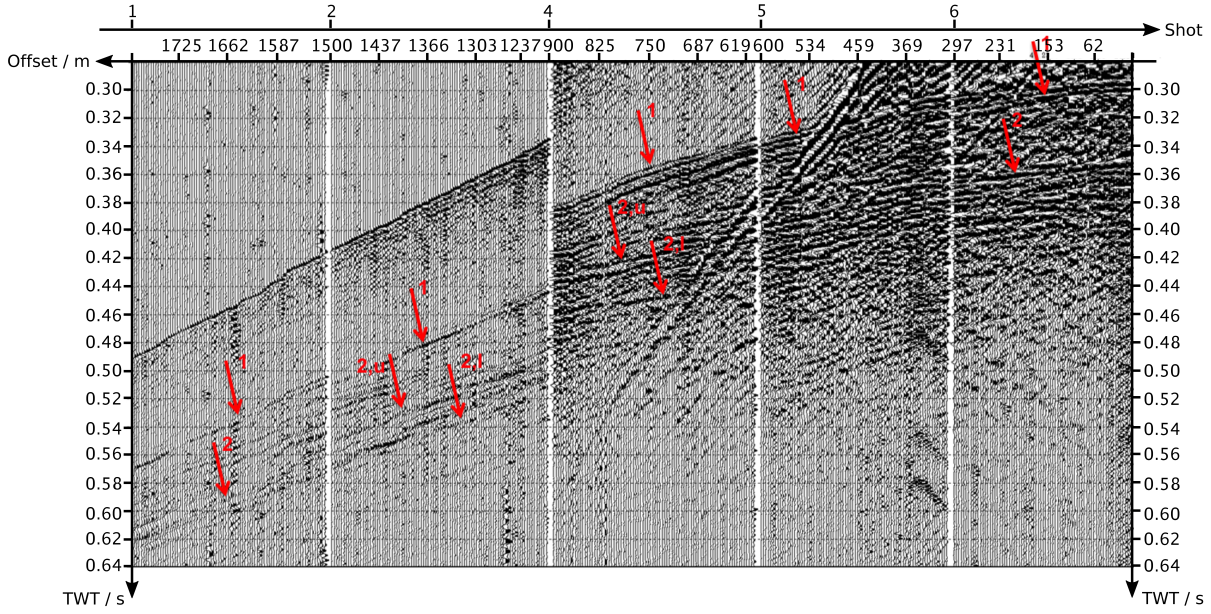

Figure 6.12: Shot sections of the CMP line 531, zoomed in. There is a data gap between s2 and s4, as no data have been recorded at s3. The red arrows with numbers 1 and 2 denote the reflection horizons picked for the application of Dix' method.

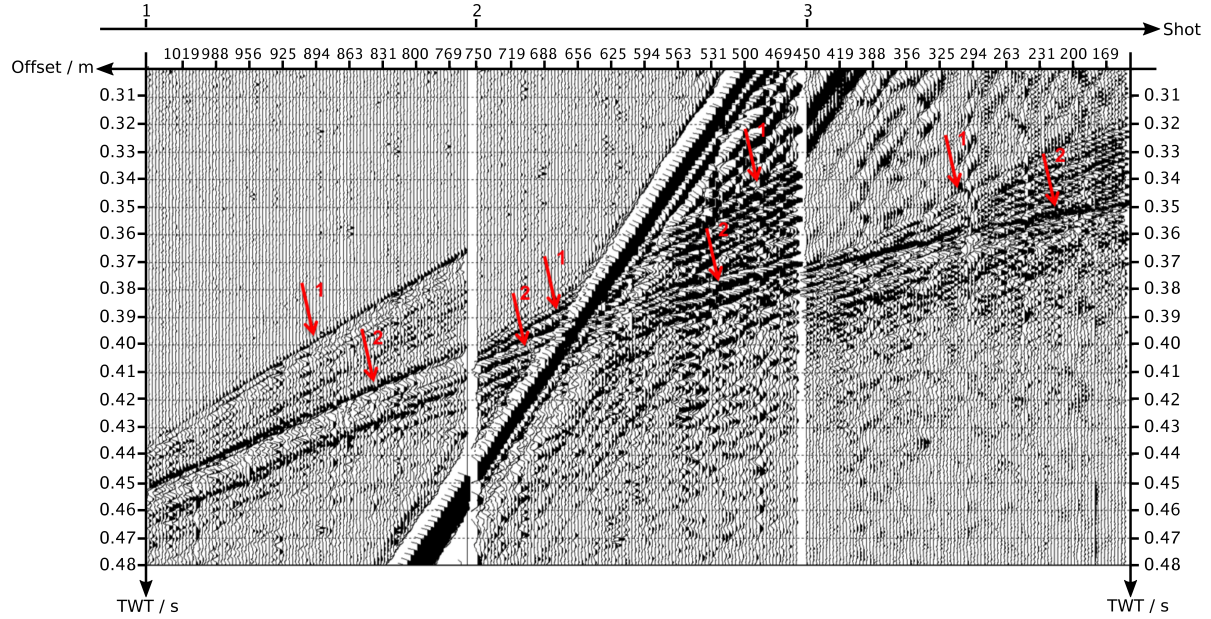

Figure 6.13: Shot sections of the CMP line 532, zoomed in. The red arrows with numbers 1 and 2 denote the reflection horizons picked for the application of Dix' Method.

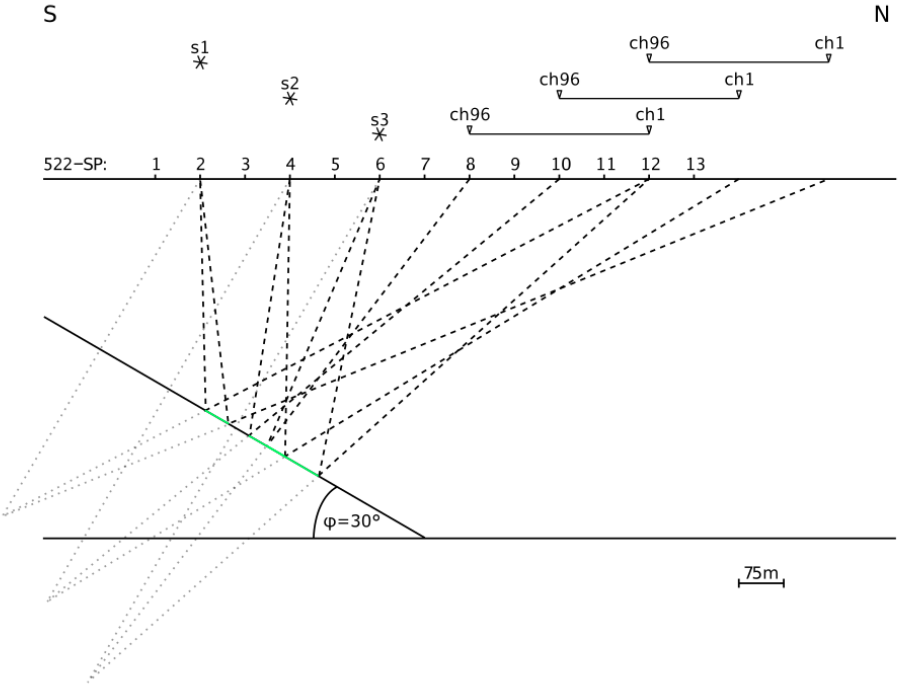

Figure 6.14: Ray paths of the reflected wave at the first layer boundary in the geometry of 532, incorporating the mean slope of 30°. The covered CDP areas of the three shots s1, s2 and s3 are colored in green.

follow as:

$$\varphi_{531} = 4.81^\circ \approx 5^\circ \tag{6.2}$$

and

$$\varphi_{532} = 30.32^\circ \approx 30^\circ \ . \tag{6.3}$$

It should be noted that the dip of the reflector of 532 has been determined from the traces of the shot of line 522 at SP5; considering the entire extent of the reflector in the range between SP1 and SP7, the dip varies from 20° to 30°.
Figure 6.14 illustrates the reflection area covered by the CMP dataset 532, taking the determined 30° dip into account. For this sketch, the reflector's depth has been estimated from the migrated stack of 522, multiplying half the TWT of several traces in the considered area with the seismic velocity in the surface ice $v_{ice,surf}$. The reflector's depth amounts approximately to 600 m at SP7 of line 522.
In Fig. 6.14, the locations of the 532 shots (s1, s2, s3) and the streamer (running from ch96 to ch1) in the CMP geometry are depicted above the SP numbers of the profiling line 522 for the benefit of clarity. It is visible that, in contrast to the initial planned geometry (see Fig. 5.3), the reflection area of the three shots doesn't coincide completely because of the reflector's dip.

As the dip of the first layer boundary in the case of line 531 amounts to only 5°, it is neglected as its influence on the determined velocity is small in comparison with the achieved accuracy.

Figure 6.15 shows the resulting x^2-t^2 diagram for the 531 data, including the regression lines created separately for the data of each shot as well as the associated velocity values calculated with Eq. (4.24). The separate analysis of each shot's data is chosen because it is not certain whether the events picked from the five different shot gathers are coherent or not.
As visible in Fig. 6.15, the regression lines from the small-offset shots s6 and s5 of line 531 cover a smaller offset interval than the lines of s1, s2 and s4, due to the fact that the reflection event was superimposed by the small-offset noise (esp. s6) and the direct S-wave signal (in the case of s5, see Fig. 6.12), respectively.

To take the 30° dip of the reflection area of line 532 into account as it is explained in section 4.3.6, the depth d_P of a reflector point P is required.
The ice-bed reflection at CMP 251 has a TWT of 246.5 ms (see Fig. 6.11). Its CMP coordinate amounts to

$$P = 250 \cdot \Delta c = 390.625\,\mathrm{m} \tag{6.4}$$

with the CMP spacing Δc. The associated depth is

$$d_P = \frac{246.5\,\mathrm{ms}}{2} \cdot v_{ice,surf} = 456.025\,\mathrm{m}\ . \tag{6.5}$$

The shot locations S of s1, s2 and s3 are computed by multiplying their CMP locations visible in Fig. 5.3 by Δc.
Figure 6.16 shows the x'^2-t^2 diagram of the 532 data, as well as the regression lines for the three shots and velocity values v_{s1}, v_{s2} and v_{s3} calculated as reciprocal roots of the lines' slopes.
As the identification of the same reflection event at s2, after it was intersected by the direct S-wave (see Fig. 6.13), was problematic, two separate regression lines are created in Fig. 6.16 and thus, also two velocity values $v_{s2,a}$ and $v_{s2,b}$ are calculated.

To determine the seismic velocity in the layer between the first and second reflector, the x-t pairs associated with the second reflector visible in Figs. 6.12 and 6.13 are picked.
As the second reflector cannot be tracked continuously in the stacks of 511 and 522, it is not possible to determine the reflection area and dip of the reflector as done above for the first reflector. Therefore, the topography of the second reflector is neglected with both the 531 and the 532 data.
Figures 6.17 and 6.18 show the squared x-t values of the second reflection picked from the 531 and 532 shot gathers as well as the associated regression lines. As explained in section 4.3.5, the reciprocal root of the lines' slopes A_2 equals the rms velocity $v_{rms,2}$ of the second layer (see Eq. (4.24)).
As it was difficult to follow the coherent reflection events associated with the second reflector continuously through all traces of a shot record in the 531 dataset, the offset range over which the regression lines are created is often short in Fig. 6.17. In the shot gather of s5, the second reflection was not picked because of its bad resolution.

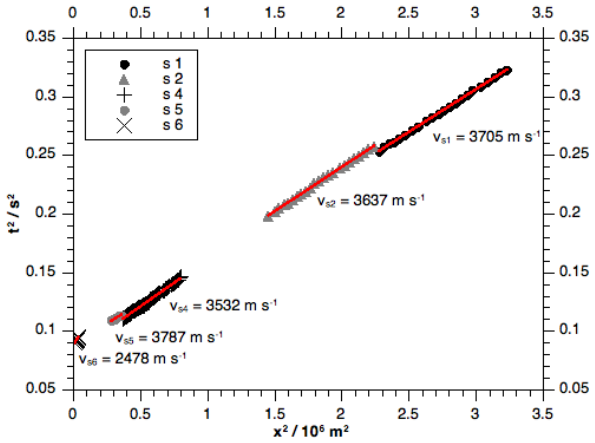

Figure 6.15: x^2-t^2 diagram to determine the seismic velocity of the ice layer from the 531 dataset, neglecting the 5° dip of the reflector. v_{s1} to v_{s6} denote the values of $v_{rms,1}$ calculated from the regression lines' slopes.

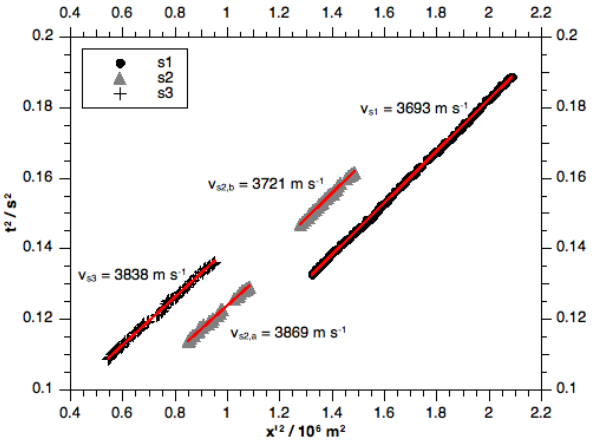

Figure 6.16: x'^2-t^2 diagram to determine the seismic velocity of the ice layer from the 532 dataset, incorporating the 30° dip of the reflector. v_{s1} to v_{s3} denote the values of $v_{rms,1}$ calculated from the regression lines' slopes.

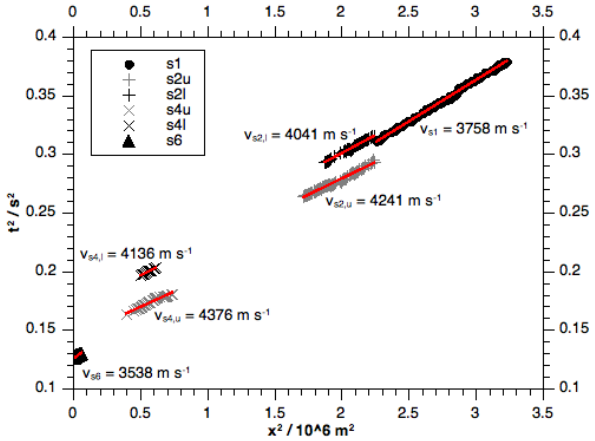

Figure 6.17: x^2-t^2 diagram to determine the seismic velocity of the second layer from the 531 dataset. v_{s1} to v_{s6} denote the values of $v_{rms,2}$ calculated from the regression lines' slopes.

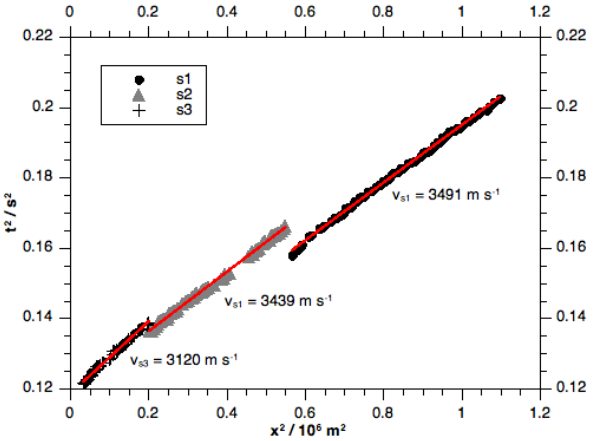

Figure 6.18: x^2-t^2 diagram to determine the seismic velocity of the second layer from the 532 dataset. v_{s1} to v_{s3} denote the values of $v_{rms,2}$ calculated from the regression lines' slopes.

7 Results

7.1 Profiling Lines 582, 511 and 522

As seen in the stacked data from line 582 displayed in Fig. 6.1 and 6.2, no reflected waves are visible in the vibroseis data.

The migrated stack from line 511 displayed in Fig. 6.9 reveals a continuous reflection horizon approximately in the range from $t = 0.28\,\mathrm{s}$ to $t = 0.34\,\mathrm{s}$. It is linearly up-dipping to the west between SP1 and SP21, and shows a rough topography including a few troughs further along the line. Also it reveals a stratification which is e.g. distinct in the range of SP 9-10.
The polarity of this reflector can best be determined in the stack (Fig. 6.8), as through the migration, the phase information is not completely preserved. It is mostly positive, as its arrivals appear black-colored. In the CMP intervals 1220-1305 and 1448-1596, the polarity becomes negative, which is indicated by the reflection onsets to be white-colored. In these two areas, the reflector dips towards west.
In the three intervals CMP 590-1110 (I), CMP 1750-2270 (II) and CMP 2880-3126 (III), a second reflector below the first is visible. In interval I, it runs parallel to the upper one and has a positive polarity. In the intervals II and III, the second reflector is slightly synclinal-shaped, with a negative polarity in II and a positive polarity in III.

In the migrated stack of line 522 displayed in Fig. 6.11, one reflector down-dipping northward with an average slope of 30° is visible between SP1 and SP7. The slope is least at the beginning of the line in the south and becomes larger to the north. An other reflector which is almost flat, smoothly dipping northward, is resolved from SP5 to the end of the line at SP13.
As seen in the unmigrated stack of the 522 dataset displayed in Fig. 6.10, the polarity of both reflectors is positive.

7.2 CMP Lines 531 and 532

Table 7.1 shows the results of Dix' method applied at the CMP datasets 531 and 532 in section 6.3.
$v_{rms,1} = v_1$ denotes the interval velocity of the topmost layer which consists of ice as the experiment has been performed on a glacier. For the determination of $v_{rms,1}$, the 5° slope of the 531 reflection area (which is located between SP44 and SP47 of line 511) has been neglected. The 30° slope of the 532 reflection area (which is approximately between SP2 and SP5 of line 522) has been incorporated using the

line	531					532		
shot	s1	s2	s4	s5	s6	s1	s2	s3
$v_{rms,1}/\mathrm{m\,s^{-1}}$	3705	3637	3532	3787	2478	3693	3869, 3721	3838
$t_1(0)/\mathrm{s}$	0.296	0.298	0.285	0.299	0.298	-	-	-
$v_1/\mathrm{m\,s^{-1}}$	3705	3637	3532	3787	2478	3693	3869, 3721	3838
$R^2(1)$	0.9995	0.9991	0.9972	0.9841	0.9847	0.9997	0.9967, 0.9972	0.9988
$v_{rms,2}/\mathrm{m\,s^{-1}}$	3758	4041, 4241	4136, 4376	-	3538	3491	3439	3120
$t_2(0)/\mathrm{s}$	0.389	0.410, 0.423	0.379, 0.409	-	0.355	-	-	-
$v_2/\mathrm{m\,s^{-1}}$	3922	4958, 5416	5581, 5873	-	6772	-	-	-
$R^2(2)$	0.9978	0.9874, 0.9925	0.9654, 0.9841	-	0.9590	0.9984	0.9984	0.9946

Table 7.1: The rms velocities $v_{rms,i}$ and zero-offset TWTs $t_i(0)$ determined from the 531 and 532 data applying Dix' method. For the $v_{rms,1}$ values of 532, a dip correction to take into account the 30° slope of the first reflector has been applied. v_1 and v_2 denote the appurtenant interval velocities. v_1 equals $v_{rms,1}$; v_2 is calculated using Eq. (4.25). $R^2(1)$ and $R^2(2)$ denote the coefficient of determination which is a measure for the regression's accuracy.

method deduced in section 4.3.6.
For the determination of $v_{rms,2}$, no dip correction has been applied at both the 531 and the 532 line. To calculate the interval velocity v_2 of the second layer in the case of the 531 results, Eq. (4.25) was used inserting the $v_{rms,1}$, $t_1(0)$ and $t_2(0)$ values from the same shot. $t_1(0)$ and $t_2(0)$ denote the zero-offset TWTs and were calculated as root of the regression lines' axis intercept.
As $t_1(0)$ and $t_2(0)$ involved in Eq. (4.25) are position-dependent in the case of the 532 data because of the first reflector's dip in the associated reflection area, no v_2 values could be determined there.

The quality of the linear fit of the values used for the particular regression lines is quantified by the coefficient of determination $R^2(i)$ listed in Tab. 7.1 for both the $i = 1$st and $i = 2$nd reflector.
The lower values of $R^2(1)$ at s5 and s6 of line 531 and of $R^2(2)$ at s4 and s6 of line 531 are caused by the small offset covered by the appurtenant regression lines (see Figs. 6.15 and 6.17) and denote a worse linear fit.

The determined P-wave velocities for the ice layer lie in the range of approx. $2500\,\mathrm{m\,s^{-1}}$-$3900\,\mathrm{m\,s^{-1}}$, the P-wave velocities for the below layer in the range of approx. $3900\,\mathrm{m\,s^{-1}}$-$6800\,\mathrm{m\,s^{-1}}$, the latter values determined from the 531 data only.
The reliability of the particular values is evaluated in the following chapter 8, where the interval velocity model used for the NMO correction in section 6.2 is derived.

8 Interpretation

8.1 ELVIS III data

In the processed ELVIS III dataset 582, no reflection energy could be resolved. The processed and stacked data of the 2-fold dataset as well as the 10-fold dataset only reveal noise, which is shown in the figures 6.1 and 6.2. This suggests that the energy introduced in the earth by the minivibrator source ELVIS is too low to arrive the earth's surface after being reflected at the ice bulk's bottom, the depth of which amounts approximately to 500-600 m.

8.2 Velocity Model

In this section, the interval velocity model along the mean line 511 from which the stacking velocity model used to correct the 511 traces for NMO is derived. Therefore, the results of the velocity analysis conducted in section 6.3 are evaluated. As only the first reflector is continuously visible along the 511 line, a two-layer stratigraphy with the glacier ice being the topmost layer is modeled. The lower reflection events are treated as local material transitions.
After an overview of the inaccuracies occurred during the velocity analysis in section 8.2.1, the reliability and accuracy of the determined velocity values are evaluated in section 8.2.2, with the objective to gain a final velocity model of the survey area's subsurface.

8.2.1 Overview of the inaccuracies occured by the application of Dix' Method

By applying Dix' method for the velocity analysis, several inaccuracies influencing the resulting velocity values occurred:
First of all, the identification of the reflection horizons in the shot gathers of 531 and 532 is restricted by personal judgment, especially the identification of coherent events associated with the second reflector in the 531 shot sections was not distinct as seen in Fig. 6.12. Compared to this accuracy to identify the events, the picking accuracy amounting to 0.5 ms is negligible.
Generally, difficult judgeable inaccuracies are involved by assuming the reflection energy visible in the seismic data coming from the vertical plane running through the particular seismic line: As seismic waves propagate as spherical waves, they can also be reflected with an offset with respect to the line.
Additional inaccuracies applying Dix' method result from the assumptions implied

by taking the lines' slopes of the squared travel time equation to compute v_{rms} values with Eq. (4.24). On the one hand, as it is explained in section 4.3.5, Eq. (4.23) is only valid in the case of $i = 1$ and, under the assumption of small spread, in the case of $i > 1$. Using the rule of thumb that x should be less than the reflector depth which is in the range of 600 m, s1, s2 and s4 of line 531 and s1 of line 532 have too large offsets to be used for velocity analysis of the second layer.
On the other hand, as it is visible in the Figs. 6.9 and 6.11, the displayed layer boundaries reveal topography and thus do not satisfy the assumption of horizontal stratification. As a consequence of non-horizontal layering, the reflection areas of the different shots within both the 531 and the 532 dataset are not the same, which influences the particular velocity values determined with Dix' Method.
When incorporating the average dip of a reflector, the determination of its slope φ as well as the reflector depth d_P yield more inaccuracies: For both values, a preliminary velocity value is required which has to be determined with another method. In the current evaluation, the seismic velocity in the near-surface ice $v_{ice,surf}$ (see Eq. (6.1)) was used which doesn't necessarily equal the average velocity of the ice pack and therefore yields additional inaccuracies. For the determination of φ and d_P, TWTs from the unmigrated and the migrated stacks, respectively, of the profiling lines were used, the values of which are influenced by the picking inaccuracy on the one hand and the static corrections involved in the stacks on the other hand. Thus, the correction of Dix' method for dipping reflectors deduced in section 4.3.6 using the non-symmetrical geometry of the current survey yields several sources of error which are to be incorporated in the interpretation of the resulting values.
Finally, with Dix' method, only average interval velocities of the subsurface material between visible layer boundaries can be determined, incorporating the inhomogeneity of the real geologic layers. In the current data, especially the presence of water-filled drainage channels and crevasses have an influence on the determined rms velocity values.

8.2.2 Derivation of the used interval velocity model along line 511

Seismic velocity in the ice layer:
The P-wave velocities $v_{rms,1} = v_1$ in the ice layer determined with Dix' method are listed in Tab. 7.1. The velocity values determined from the shots s5 and s6 of line 531 are not interpreted further as the associated regression lines (see Fig. 6.15) cover a relatively small offset range.
The v_1 values determined from line 532, where the layer boundary below the ice is steeply dipped, are first of all associated with different reflection areas, as it is mentioned in the previous section 8.2.1. Although the reflection area range of this line has been determined in Fig. 6.14, taking the 30° dip angle into account, the exact reflection area remains unknown as even within the same shot record, the reflector dip varies and its depth could only be estimated from the TWT in the migrated section of 522 using a preliminary assumed seismic velocity.
For these reasons, only the results from the shots s1, s2 and s4 of line 531 are representative to derive v_1. It follows from the three rounded values v_{s1}, v_{s2} and v_{s3} that v_1 lies between $3500\,\mathrm{m\,s^{-1}}$ and $3700\,\mathrm{m\,s^{-1}}$. As the resolutional quality of the

unmigrated stack of 511 isn't conclusive in what is the best stacking velocity model to use for NMO correction, v_1 can't be determined more accurately with the help of the used data analysis methods.
The derived velocity range for v_1 thus includes lower values than the velocity in the surface ice $v_{ice,surf}$. Looking at the reflection area SP44-47 in the stack of line 511 (Fig. 6.8), the reflector is less resolved there than e.g. from SP1 to SP39. This could be induced by water content of the material in this area, attenuating the high frequencies of the signal which yields a decreased resolution of the reflector as well as a decreased seismic velocity.
As the mentioned weakness of 531's reflection area is only a local feature, the velocity range from 3500-3700 $\mathrm{m\,s^{-1}}$ isn't necessarily representative with regard to the average P-wave velocity in the ice of the complete survey area.
In the interval velocity model underlying the stacking velocity model used to correct the traces of the profiling lines for NMO,

$$v_{ice} = 3500\,\mathrm{m\,s^{-1}} \tag{8.1}$$

is used as interval velocity of the ice layer. As mentioned above, the resolution of the resulting stacks doesn't increase by using the upper range value for the seismic velocity, $v_{ice} = 3700\,\mathrm{m\,s^{-1}}$.

Seismic velocity in the second layer:
The seismic velocity v_2 of the material lying below the ice mass is firstly tried to be determined from the x^2-t^2 diagrams displayed in Figs. 6.17 and 6.18.
The $v_{rms,2}$ values resulting from line 531 are not reliable because of the small covered offset interval in the case of s4 and s6, and because of the large absolute offsets which violate the small-spread assumption in the case of s1 and s2.
The influence of the 30° dipped first layer boundary on the $v_{rms,2}$ values resulting from line 532 is unknown. That is because the exact ray paths can't be reconstructed due to the inaccurate determinability of the exact slope and depth of the reflector. As a result, the correction for Eq. (4.25) required to calculate the interval velocity v_2 is unknown, as the included zero-offset TWT are not constant in the dipped case. To summarize, the application of Dix' method on the CMP datasets 531 and 532 didn't provide a reliable interval velocity for the second layer. Therefore, the material lying below the ice mass is determined from structural features and the polarity of the first reflection both visible in the 511 stack.

Subglacial structure:
The shape of the first reflection horizon visible in the 511 stack, Fig. 6.8, is characterized by a rough topography, with smoothly alternating dips. It also doesn't appear as single hard event, but shows some stratigraphy. These features are a hint for subglacial sediments deposited below the glacier.
The sign of the reflection coefficient R associated with the layer boundary between the first and the second layer equals the polarity of the first reflection event determined in section 7.1. In the following part, the changes of sign of R are reconstructed in order to estimate the density and P-wave velocity of the second layer. Therefore, the material classification for the NEGIS region, northeast Greenland, given by Christianson et al. (2014) is used. The appurtenant parameteres are listed in Tab. 8.1.

Material	v_P/m s^{-1}	ρ / kg m^{-3}
Ice	3840	917
Lithified sediment/crystalline basement	3000-6200	2200-2800
Consolidated sediments	2000-2600	1600-1900
Unconsolidated sediments/lodged till	1700-1900	1600-1800
Dilatant till	1600-1800	1600-1800
Water	1498	1000

Table 8.1: P-wave velocities v_P and densities ρ of the ice and possible subglacial bed materials given by Christianson et al. (2014) for the upper NEGIS region, northeast Greenland.

Polarity of the reflection coefficient:
In the geometry of the profiling lines depicted in Fig. 5.2, the maximum angle of incidence is

$$\theta_{max} = \arctan\left(\frac{x_{max}}{2 \cdot d}\right) \approx 15^\circ \tag{8.2}$$

with the maximal offset $x_{max} \approx 319\,\mathrm{m}$ and the reflector depth $d \approx 600\,\mathrm{m}$ which has been estimated in section 6.3. To calculate the reflection coefficient R, the Zoeppritz equations mentioned in section 4.3.4 are neglected implying $\theta \approx 0^\circ$, so that Eq. (4.17) is used to calculate R.
The therefore used density of the ice layer $\rho_1 = 917\,\mathrm{kg\,m^{-3}}$ (Tab. 8.1) is given by Christianson et al. (2014). For v_1, the above determined boundary values $3500\,\mathrm{m\,s^{-1}}$ and $3700\,\mathrm{m\,s^{-1}}$ are used. The material parameters for the second layer are extracted from Tab. 8.1, combining ρ_2-v_2 pairs which are possible according to Christianson et al. (2014).
Table 8.2 shows the resulting values for R using $v_1 = 3500\,\mathrm{m\,s^{-1}}$. The equivalent table using $v_1 = 3700\,\mathrm{m\,s^{-1}}$ is given in the appendix 10.1 and reveals the same signs of the resulting R values.
The material parameters of lithified sediments/crystalline basement and consolidated sediments yield, apart from one exception, positive values of R; changes of sign appear for unconsolidated sediments/lodged till and dilatant till. Assuming a sediment density of ρ_2=1800 kg m^{-3}, the sign of R becomes negative between $v_2 = 1700\,\mathrm{m\,s^{-1}}$ and $1800\,\mathrm{m\,s^{-1}}$. With a density of ρ_2=1700 kg m^{-3}, the polarity change of R takes place between $v_2 = 1800\,\mathrm{m\,s^{-1}}$ and $1900\,\mathrm{m\,s^{-1}}$. That is, the change of sign of R can be explained by unconsolidated sediments or dilatant till lying below the ice mass.

Interpretation:
The possibility that stronger material such as consolidated or lithified sediments lie under the ice mass, with the negative R values induced by local meltwater channels, is excluded for the reason that in the vicinity of the negative reflection areas, the positive reflector doesn't appear very strong.

For the searched interval velocity model, $v_2 = 1800\,\mathrm{m\,s^{-1}}$ is used in the areas where $R > 0$ and $v_2 = 1700\,\mathrm{m\,s^{-1}}$ is used in the areas where $R < 0$, assuming a density of $\rho_2 = 1800\,\mathrm{kg\,m^{-3}}$.

$v_2/\mathrm{m\,s^{-1}}$ \ $\rho_2/\mathrm{kg\,m^{-3}}$	1000	1600	1700	1800	1900	2200	2400	2600	2800
1498	-0.364								
1600		-0,113	-0,083	-0,054					
1700		-0,083	-0,052	-0,024					
1800		-0,054	-0,024	0,005					
1900		-0,027	0,003	0,032					
2000		-0,001	0,029	0,057	0,084				
2100		0,023	0,053	0,082	0,108				
2200		0,046	0,076	0,105	0,131				
2300		0,068	0,098	0,127	0,153				
2400		0,089	0,119	0,147	0,174				
2500		0,110	0,139	0,167	0,194				
2600		0,129	0,159	0,186	0,212				
3000						0,346	0,383	0,417	0,447
3840						0,449	0,483	0,513	0,540
5000						0,548	0,578	0,604	0,627
6200						0,619	0,645	0,668	0,688

Table 8.2: Values for the reflection coefficient R resulting by using Eq. (4.17). For the upper layer, $\rho_1 = 917\,\mathrm{kg\,m^{-3}}$ and $v_1 = 3500\,\mathrm{m\,s^{-1}}$ are inserted, for the lower layer, different P-wave velocities v_2 and densities ρ_2 which are given by Christianson et al. (2014) and listed in Tab. 8.1 are used.

Figure 8.1 illustrates the P-wave velocity model in CMP-TWT coordinates along the profiling line 511, incorporating the seismic velocities of the first two layers derived up to here. The topmost layer consists of the temperate glacier ice with the density $\rho_1 = 917\,\mathrm{kg\,m^{-3}}$ and the P-wave velocity $v_1 = 3500\,\mathrm{m\,s^{-1}}$, the second layer consists of the subglacial sediments with the modeled density $\rho_2 = 1800\,\mathrm{kg\,m^{-3}}$ and the P-wave velocities $v_1 = 1700 - 1800\,\mathrm{m\,s^{-1}}$. The lateral structure is extracted from the stack of 511.

8.3 Structural Model

In this section, the subsurface structures visible in the stacks of the profiling lines 511 and 522, which were described in section 7.1, are interpreted with regard to possible subglacial phenomena present in the survey area. As the reflectors are less resolved in the migrated stacks, the unmigrated stacks of both lines are used for structural interpretation.
Figures 8.2 and 8.3 reveal the stacks of 511 and 522, the observed reflection events colored. As determined in the previous section 8.2, the continuous reflection horizon visible in the 511 dataset (orange-colored in Fig. 8.2) is induced by the boundary between the ice mass and the subjacent sediments. As the associated TWT at the intersection of the 511 and 522 profile coincides with the TWT of the reflector seen in the 522 stack (Fig. 8.3), it can be inferred that the same reflector is depicted in both datasets.

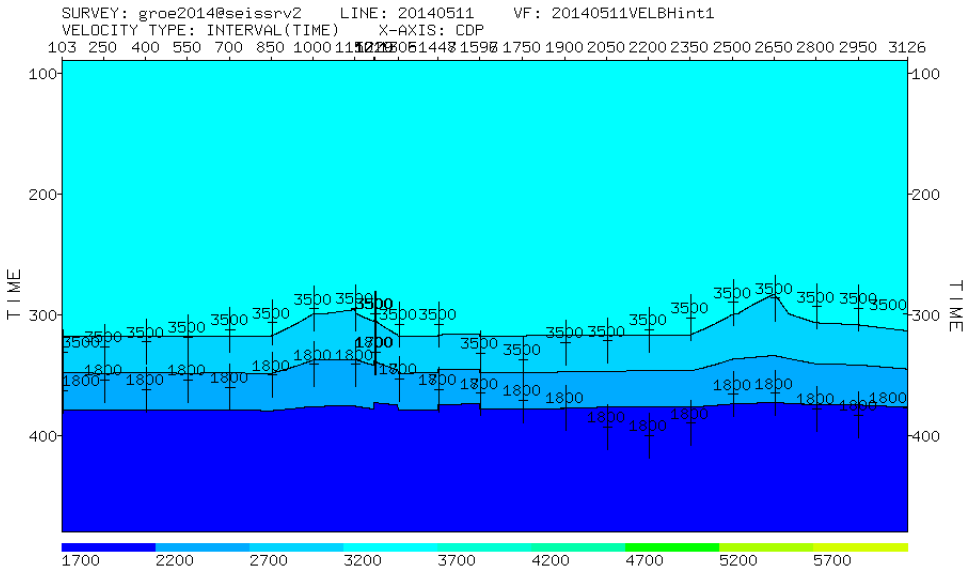

Figure 8.1: Velocity model along line 511 which was used to derive the stacking velocities used for NMO correction in section 6.2.

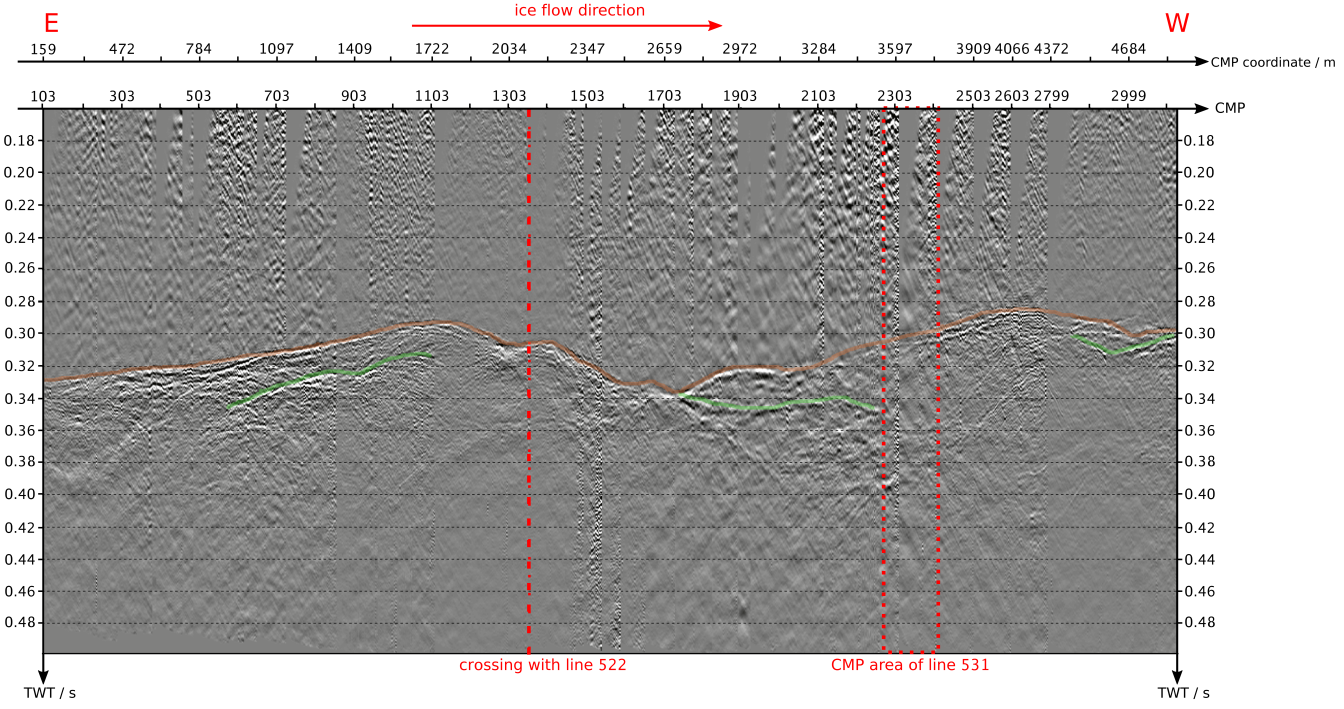

Figure 8.2: Unmigrated stack of the 511 data with the first, continuous reflector marked in orange, and the three second, local reflection horizons marked in green.

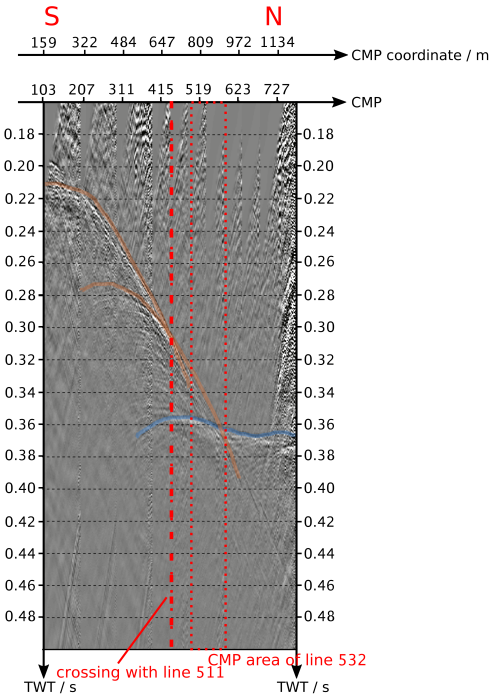

Figure 8.3: Unmigrated stack of the 522 data with the reflector which is coinciding with the one seen in the 511 stack (Fig. 8.2) marked in orange and the second reflection horizon marked in blue. In contrast to the Figs. 6.10 and 6.11, the scale is here adjusted to the scale of Fig. 8.2.

With the velocity model for line 511 determined in the previous section 8.2, the depths of the layer boundaries visible in the seismic data can be calculated. For the ice velocity v_1, the lower and higher range boundary $3500\,\mathrm{m\,s^{-1}}$ and $3700\,\mathrm{m\,s^{-1}}$ are used.
The depth of the narrowest part of the ice-sediment boundary along line 511 amounts to

$$d^{511}_{1,min} = \frac{t_{1,min}}{2} \cdot v_{ice} = \frac{284\,\mathrm{ms}}{2} \cdot \left\{3500\,\mathrm{m\,s^{-1}}; 3700\,\mathrm{m\,s^{-1}}\right\} = \{497\,\mathrm{m}; 525\,\mathrm{m}\} \approx 500\,\mathrm{m} \tag{8.3}$$

which appears at CMP 2611. The depth of the deepest part (CMP 1736) results respectively to $d^{511}_{1,max} \approx 600\,\mathrm{m}$.

The depth interval between the first reflector and the second which is appearing in interval I (CMP 590-1110, see section 7.1) on line 511 amounts approximately to

$$\Delta d^{511}_{I} = \frac{|t_1 - t_2|}{2} \cdot v_{sed} = \frac{22.5\,\mathrm{ms}}{2} \cdot 1800\,\mathrm{ms} = 20.3\,\mathrm{m}\ . \tag{8.4}$$

The maximal thickness of the sediment layer visible in interval II (CMP 1750-2270) of line 511 amounts to

$$\Delta d^{511}_{II,max} = \frac{|t_1 - t_2|}{2} \cdot v_{sed} = \frac{22.9\,\mathrm{ms}}{2} \cdot 1700\,\mathrm{ms} = 19.5\,\mathrm{m}\ , \tag{8.5}$$

which is found in the middle of the lens-shaped interspace between the first and the second reflector, i.e. at CMP 1916.
The equivalent thickness in the middle of the lens-shaped interspace in interval III (CMP 2880-3126) amounts at CMP 2957 to

$$\Delta d^{511}_{III,max} = \frac{|t_1 - t_2|}{2} \cdot v_{sed} = \frac{18.1\,\text{ms}}{2} \cdot 1800\,\text{ms} = 16.3\,\text{m}\ . \tag{8.6}$$

The second reflector in interval I visible in the stack of the 511 data runs parallel to the ice-sediment boundary as described in section 7.1. Because of their parallelism and resemblance, the development of the sediment layer and the lower material seems correlated. On top of that, the second reflection event is less distinct than the first, and therefore it can be excluded to be the metamorphic bedrock. That is why the lower material is likely to be a more consolidated sediment than the upper lying till.

The negative sign of the reflection coefficient R mentioned in section 7.1 appears on the first reflector in the two intervals CMP 1220-1305 and CMP 1448-1596 which both are on the lee side of the first anticlinal structure of the above reflector. Secondly, R is negative at the synclinal-shaped lower reflection event in the interval II (CMP 1750-2270).
Both polarity changes can be explained with meltwater accumulating in the shadow zone of the ice flow in the first and in a trough in the second case.

The ice-sediment boundary which is orange-colored in the 522 stack (Fig. 8.3) and the second reflector marked in blue can first of all be separated because they intersect, which takes place around CMP 570. As the strength of the second (blue-colored) reflector is lower than that of the first reflector, which is visible in Fig. 6.10, it can be excluded to be the ice-bedrock contact, but interpreted as another sediment layer.

The orthogneiss, which is the bedrock below Russell Glacier as mentioned in section 3.2.2, has not been observed in the seismic data. For this reason, the depth of the bedrock in the survey area can merely be specified as being greater than the depth of the visible reflectors, i.e. greater than approximately 500-600 m.

9 Conclusion

As mentioned in section 8.1, the energy of the minivibrator source ELVIS III has not been sufficient to resolve the approximately 500-600 m deep ice-bed contact of Russell Glacier.
From that, it can be inferred that the application of ELVIS is not useful to investigate subglacial features of huge-depth polar glaciers, but its use is limited to shallower depths. To use the vibroseis technique for this purpose anyway, vibrator sources providing greater energy are required.

As the ice-sediment transition in the survey area has a considerable topography that is displayed in the stacks of the profiling lines 511 and 522, the application of Dix' method on the existing CMP data in section 6.3 resulted in very varying velocity values. Additionally to the enumeration of inaccuracies occured in the velocity analysis in section 8.2.1, the general applicability of the method derived in section 4.3.6 to correct Dix' Method for dip is evaluated now. As the derived method has the lack that it requires a preliminary velocity to determine the velocity value itself, it is based on a circular reasoning. To use it nevertheless, an iterative procedure could be possible. However, the included model assumptions such as the homogeneity of the layers and the constancy of the reflector's slope are a persistent drawback of the method.
For future applications of Dix' method on CMP data in the case of a topographic layer boundary, it would be more productive to choose the CMP area in the field with the help of a look on a preliminary processed seismic profiling dataset to derive horizontal parts of the displayed reflector (e.g. the northern half of the 522 dataset, see Fig. 6.11). This method would provide higher accuracies, as no correction for dip would be necessary. In the case of a reflector with a constant slope, the application of the method provided by Dix (1955) for a dataset with stationary source-receiver midpoints (see section 4.3.6) is possible. With respect to the used datasets 531 and 532 in this thesis, the data of more shots in the CMP geometry would have been required to apply Dix' dip correction, in order to have more traces with the same CMP.
Moreover, the investigation of the subglacial structures and the reflectors' polarity, both visible in the seismic stacks of the profiling lines 511 and 522, has been conclusive with regard to the determination of the subglacial material, why it can be recommended to be used to improve seismic velocity analysis.
A more precise velocity analysis using the existing CMP datasets 531 and 532 is possible by applying amplitude-versus-offset (AVO) analysis. In addition to the consideration of the polarity of the reflection coefficient R, the absolute values of R can be determined more accurate by this method.

Regarding the investigation of the subglacial bedforms present in the survey area, it was not possible to derive a 3D model in the framework of this thesis, as only two

seismic cross-sections were derived. Therefore, a 3D high resolution model would be required.

10 Appendix

10.1 To section 8.2: R values using the higher value for the P-wave velocity in ice

Table 10.1 reveals the values of the reflection coefficient R, calculated as the values in Tab. 8.2 but used $v_1 = 3700\,\mathrm{m\,s^{-1}}$ for the P-wave velocity of the ice layer.

$v_2/\mathrm{m\,s^{-1}}$ \ $\rho_2/\mathrm{kg\,m^{-3}}$	1000	1600	1700	1800	1900	2200	2400	2600	2800
1498	-0,387								
1600		-0,140	-0,110	-0,082					
1700		-0,110	-0,080	-0,052					
1800		-0,082	-0,052	-0,023					
1900		-0,055	-0,025	0,004					
2000		-0,029	0,001	0,030	0,057				
2100		-0,005	0,025	0,054	0,081				
2200		0,018	0,049	0,077	0,104				
2300		0,041	0,071	0,099	0,126				
2400		0,062	0,092	0,120	0,147				
2500		0,082	0,112	0,140	0,167				
2600		0,102	0,131	0,159	0,186				
3000						0,321	0,359	0,394	0,425
3840						0,427	0,462	0,493	0,520
5000						0,529	0,559	0,586	0,610
6200						0,602	0,629	0,652	0,673

Table 10.1: Values for the reflection coefficient R resulting by using Eq. (4.17). For the upper layer, $\rho_1 = 917\,\mathrm{kg\,m^{-3}}$ and $v_1 = 3700\,\mathrm{m\,s^{-1}}$ are inserted, for the lower layer, different P-wave velocities v_2 and densities ρ_2 which are given by Christianson et al. (2014) and listed in Tab. 8.1 are used.

11 Acknowledgements

Firstly, I would like to thank my reviewer Prof. Dr. T. Bohlen for his support of the current thesis that took place in the framework of the research at AWI Bremerhaven.

Secondly, I would like to thank my second reviewer Prof. Dr. O. Eisen for offering me such an interesting topic of investigation, and for cooperating with Prof. Dr. T. Bohlen to grade the current thesis.

Thirdly, I would like to thank my supervisor Dr. C. Hofstede for his competent assistance and encouragement throughout the course of the work.

Last but not least, I would like to thank the members of the Glaciology group of AWI for such a warm and friendly atmosphere, and for providing me with all necessary equipment for my work.

List of Figures

List of Tables

Bibliography

Benn, D. I. and D. J. A. Evans (1998). *Glaciers & Glaciation*. Hodder Arnold Publication. Arnold. ISBN: 9780340584316.

Christianson, K., L. E. Peters, R. B. Alley, S. Anandakrishnan, R. W. Jacobel, K. L Riverman, A. Muto, and B. A. Keisling (2014). "Dilatant till facilitates ice-stream flow in northeast Greenland". In: *Earth and Planetary Science Letters*.

CREWES, University of Calgary (2005). *The CREWES Zoeppritz Explorer Applet*. online. URL: https://www.crewes.org/ResearchLinks/ExplorerPrograms/ZE/ZEcrewes.html.

Diez, A., O. Eisen, I. Weikusat, J. Eichler, C. Hofstede, P. Bohleber, T. Bohlen, and U. Polom (2014). "Influence of ice crystal anisotropy on seismic velocity analysis". In: *Annals of Glaciology*. DOI: 10.3189/2014AoG67A002.

Dix, C. H. (1955). "Seismic velocities from surface measurements". In: *Geophysics* XX.1, pp. 68–86.

Dobrin, M. B. and C. H. Savit (1988). *Introduction to Geophysical Prospecting*. 4th ed. McGraw-Hill.

Doyle, S. H., A. Hubbard, A. A. W. Fitzpatrick, D. van As, A. B. Mikkelsen, R. Pettersson, and B. Hubbard (2014). "Persistent flow acceleration wiwith the interior of the Greenland ice sheet". In: *Geophys. Res. Lett.* 41, pp. 899–905. DOI: 10.1002/2013GL058933.

Faber, K. and P. W. Maxwell (1997). "Geophone spurious frequency: What is it and how does it affect seismic data quality?" In: *Canadian Journal of Exploration Geophysics* 33.1 and 2, pp. 46–54.

Hofstede, C., O. Eisen, A. Diez, D. Jansen, Y. Kristoffersen, A. Lambrecht, and C. Mayer (2013). "Investigating englacial reflections with vibro- and explosive-seismic surveys at Halvfarryggen ice dome, Antarctica". In: *Annals of Glaciology* 54.64, pp. 189–200. DOI: 10.3189/2013AoG64A064.

Ikelle, L. and L. Amundsen. *Vibroseis sweep correlation*. online. URL: http://petroleumgeophysics.com/images/202/.

Klint, K. E. S., A. Parmenter, T. Ruskeeniemi, L. C. Liljedahl, and A. Lehtinen (2013). "Lineament mapping and geological history of the Kangerlussuaq region, southern West Greenland". In: *Geological Survey of Denmark and Greenland Bulletin* 28, pp. 57–60.

Moon, T. and I. Joughin (2008). "Changes in ice front position on Greenland's outlet glaciers from 1992 to 2007". In: *Journal of Geophysical Research: Earth Surface* 113.F2. F02022, n/a–n/a. ISSN: 2156-2202. DOI: 10.1029/2007JF000927. URL: http://dx.doi.org/10.1029/2007JF000927.

Paterson, W. S. B (1994). *The Physics of Glaciers*. 3rd ed. Vol. 1. Butterworth Heinemann, Elsevier Science.

Rignot, E. and J. Mouginot (2012). "Ice flow in Greenland for the International Polar Year 2008–2009". In: *Geophysical Research Letters* 39.11. L11501, n/a–n/a. ISSN: 1944-8007. DOI: 10.1029/2012GL051634. URL: http://dx.doi.org/10.1029/2012GL051634.

Smeets, C. J. P. P., W. Boot, A. Hubbard, R. Pettersson, F. Wilhelms, M. R. van den Broeke, and R. S. W. van de Wal (2012). "Instruments and Methods. A wireless subglacial probe for deep ice applications". In: *Journal of Glaciology* 58.211. DOI: 10.3189/2012JoG11J130.

van de Wal, R. S. W., W. Boot, C. J. P. P. Smeets, H. Snellen, M. R. van den Broeke, and J. Oerlemans (2012). "Twenty-one years of mass balance observations along the K-transect, West Greenland". In: *Earth System Science Data* 4, pp. 31–35. DOI: 10.5194/essd-4-31-2012.

van de Wal, R. S. W., C. J. P. P. Smeets, W. Boot, M. Stoffelen, R. van Kampen, S. H. Doyle, F. Wilhelms, M. R. van den Broeke, C. H. Reijmer, J. Oerlemans, and A. Hubbard (2015). "Self-regulation of ice flow varies across the ablation area in south-west Greenland". In: *The Cryosphere* 9, pp. 603–611. DOI: 10.5194/tc-9-603-2015.

Yilmaz, Ö. (2001). *Seismic Data Analysis*. Ed. by Stephen M. Doherty. Vol. 1. Society of Exploration Geophysicists.